

Mapping the NPHP-JBTS-MKS Protein Network Reveals Ciliopathy Disease Genes and Pathways

Liyun Sang,^{1,16} Julie J. Miller,^{2,16} Kevin C. Corbit,³ Rachel H. Giles,⁴ Matthew J. Brauer,¹ Edgar A. Otto,⁵ Lisa M. Baye,⁶ Xiaohui Wen,¹ Suzie J. Scales,¹ Mandy Kwong,¹ Erik G. Huntzicker,¹ Mindan K. Sfakianos,¹ Wendy Sandoval,¹ J. Fernando Bazan,¹ Priya Kulkarni,¹ Francesc R. Garcia-Gonzalo,³ Allen D. Seol,³ John F. O'Toole,⁵ Susanne Held,⁵ Heiko M. Reutter,⁸ William S. Lane,⁹ Muhammad Arshad Rafiq,¹⁰ Abdul Noor,¹⁰ Muhammad Ansar,¹¹ Akella Radha Rama Devi,¹² Val C. Sheffield,^{7,15} Diane C. Slusarski,⁶ John B. Vincent,^{10,13} Daniel A. Doherty,¹⁴ Friedhelm Hildebrandt,^{5,15} Jeremy F. Reiter,³ and Peter K. Jackson^{1,*}

¹Genentech Inc., South San Francisco, CA 94080, USA

²Department of Chemical and Systems Biology, Stanford University School of Medicine, Stanford, CA 94305, USA

³Department of Biochemistry and Biophysics, Cardiovascular Research Institute, University of California, San Francisco, San Francisco, CA 94158, USA

⁴Department of Medical Oncology and Department of Nephrology and Hypertension, University Medical Center Utrecht, Heidelberglaan 100, 3584CX Utrecht, The Netherlands

⁵Departments of Pediatrics and Human Genetics, University of Michigan, Ann Arbor, MI 48109, USA

⁶Department of Biology

⁷Department of Pediatrics,

University of Iowa, Iowa City, IA 52242, USA

⁸Institute of Human Genetics and Department of Neonatology, Children's Hospital, University of Bonn, D-53111 Bonn, Germany

⁹Mass Spectrometry and Proteomics Resource Laboratory, Center for Systems Biology, Harvard University, Cambridge, MA 02138, USA

¹⁰Molecular Neuropsychiatry and Development Lab, Neurogenetics Section, Centre for Addiction and Mental Health, Toronto, ON M5T 1R8, Canada

¹¹Department of Biochemistry, Quaid-e-Azam University, Islamabad 45320, Pakistan

¹²Rainbow Children's Hospital, Hyderabad 500 034, India

¹³Department of Psychiatry, University of Toronto, Toronto, ON M5T 1R8, Canada

¹⁴Department of Pediatrics, University of Washington, Seattle 98195, WA

¹⁵Howard Hughes Medical Institute, Chevy Chase, MD 20815, USA

¹⁶These authors contributed equally to this work

*Correspondence: pjackson@gene.com

DOI 10.1016/j.cell.2011.04.019

SUMMARY

Nephronophthisis (NPHP), Joubert (JBTS), and Meckel-Gruber (MKS) syndromes are autosomal-recessive ciliopathies presenting with cystic kidneys, retinal degeneration, and cerebellar/neural tube malformation. Whether defects in kidney, retinal, or neural disease primarily involve ciliary, Hedgehog, or cell polarity pathways remains unclear. Using high-confidence proteomics, we identified 850 interactors copurifying with nine NPHP/JBTS/MKS proteins and discovered three connected modules: “NPHP1-4-8” functioning at the apical surface, “NPHP5-6” at centrosomes, and “MKS” linked to Hedgehog signaling. Assays for ciliogenesis and epithelial morphogenesis in 3D renal cultures link renal cystic disease to apical organization defects, whereas ciliary and Hedgehog pathway defects lead to retinal or neural deficits. Using 38 interactors as candidates, linkage and sequencing analysis of 250

patients identified *ATXN10* and *TCTN2* as new NPHP-JBTS genes, and our *Tctn2* mouse knockout shows neural tube and Hedgehog signaling defects. Our study further illustrates the power of linking proteomic networks and human genetics to uncover critical disease pathways.

INTRODUCTION

Ciliopathies are a heterogeneous group of diseases that present with a broad constellation of clinical phenotypes, including renal cysts, retinal degeneration, polydactyly, mental retardation, and obesity (reviewed by Hildebrandt et al., 2009a; Zaghloul and Katsanis, 2009). Studies of these diseases suggest that their pathogenesis relates to dysfunction of the microtubule-based primary cilium. It is hypothesized that the primary cilium is a sensory organelle, acting as a mechanosensor in the kidney and organizing sensory receptors, including rhodopsin, in the retina. Cilia are also key components of the Hedgehog (Hh) signaling pathway (Corbit et al., 2005; Huangfu et al., 2003). The consistent finding of kidney, retinal, liver, limb, and brain

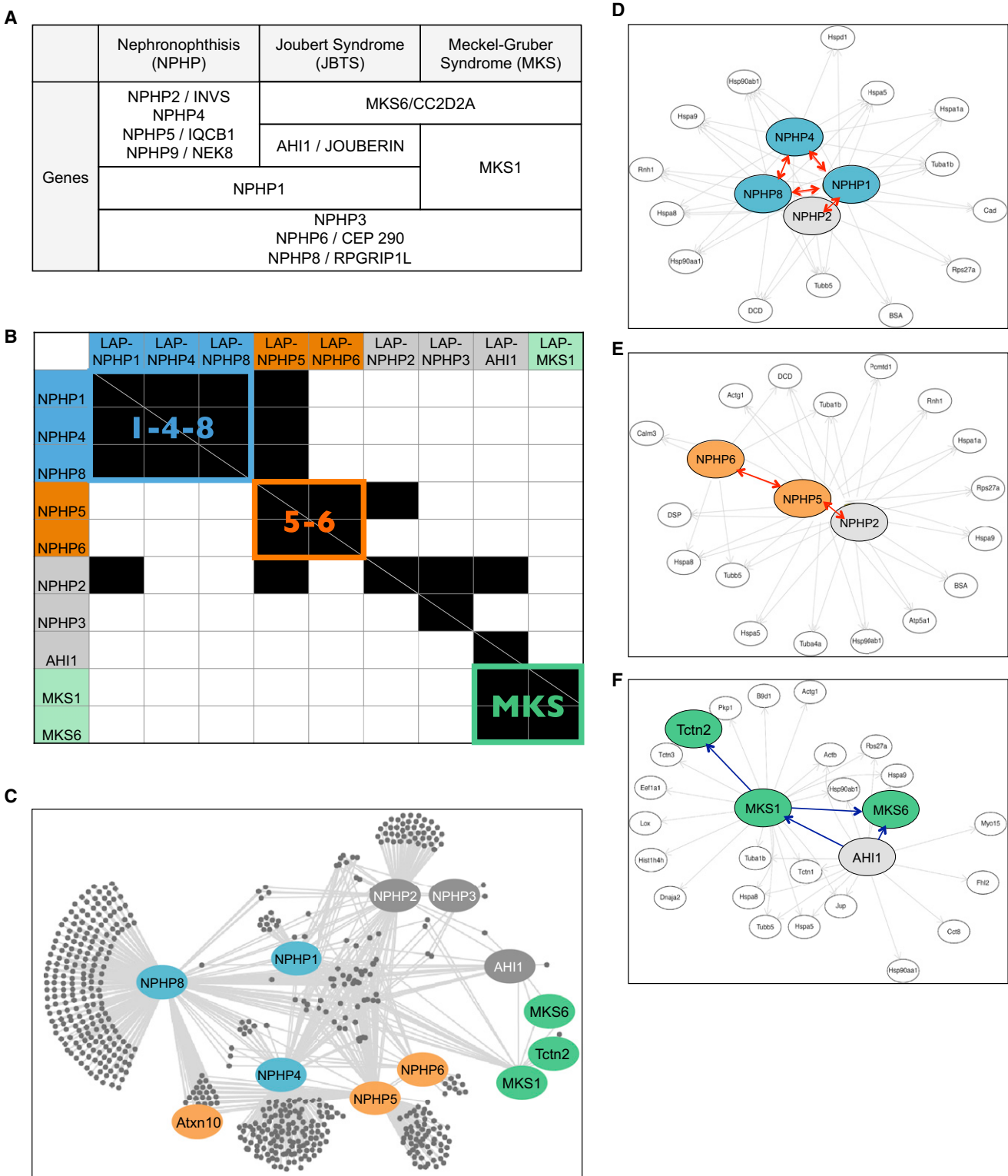


Figure 1. Mapping the NPHP-JBTS-MKS Disease Protein Network Using G-LAP-Flp Strategy

(A) List of genes mutated in NPHP-JBTS-MKS ciliopathies.

(B) Heat map summarizing MS/MS interactions among NPHP proteins discovered using G-LAP-Flp strategy. Horizontal axis, LAP-tagged "bait" proteins; vertical axis, interacting proteins. Identified interactions are shown in black. The NPHP1-4-8 (1-4-8), NPHP5-6 (5-6), and MKS modules are color coded in blue, orange, and green.

defects among the ciliopathies in turn suggests that cilia-dependent sensory and signaling functions are critical in the development, tissue organization, and physiological function of multiple organ systems. However, whether all “ciliopathies” are simply caused by the absence of cilia themselves remains unclear. Specific ciliary signaling pathways, ciliary receptors, additional ciliary effectors, or even centrosomes, may be at the root of specific types of tissue or sensory failure, and these relationships have remained elusive.

Three linked ciliopathies called Nephronophthisis (NPHP), Joubert syndrome (JBTS), and Meckel-Gruber syndrome (MKS) are autosomal-recessive disorders, initially described as distinct entities but recently found to share phenotypic overlap, notably in cystic kidney disease. Nephronophthisis is the least severe of the group, characterized primarily by renal cysts but sometimes involving retinal degeneration (called Senior-Loken syndrome), *situs inversus*, and mental retardation (Hildebrandt et al., 2009a). Joubert syndrome involves both renal and nonrenal manifestations of NPHP disease but is distinguished by cerebellar vermis aplasia, a significant malformation of the cerebellum that is linked to ataxia (Parisi et al., 2007). As a perinatal lethal disease, Meckel-Gruber syndrome is the most severe, characterized by occipital encephalocele, polydactyly, liver fibrosis, and severe renal cysts (Salonen and Paavola, 1998).

To date, mutations in 16 genes have been linked to this group of disorders: *NPHP1–9*, *AHI1/Jouberin*, *ARL13B*, *INPP5E*, *TMEM216*, *MKS1*, *MKS3/TMEM67*, and *MKS6/CC2D2A* (Tallila et al., 2008; Hildebrandt et al., 2009a; Lee and Gleeson 2010; Supplemental References). Interestingly, different alleles of the same gene can result in the phenotypic spectrum of NPHP, JBTS, and MKS. For example, *NPHP1* mutations were reported in patients with both NPHP and JBTS (Parisi et al., 2007), whereas mutations in *NPHP3*, *NPHP6/CEP290*, and *NPHP8/RPGRIP1L* are linked to all forms of disease along the NPHP-JBTS-MKS spectrum (Baala et al., 2007) (Figure 1A). Because these three diseases can be caused by mutation of the same genes, we considered the hypothesis that these disorders may link to defects in a specific set of cellular mechanisms and that the associated proteins may interact and function in common pathways. NPHP/JBTS/MKS proteins are rich in protein-protein interaction domains (Figure S1A available online), suggesting extensive protein-protein interactions. Studies using yeast two-hybrid and coimmunoprecipitation (co-IP) discovered interactions of *NPHP1* with *NPHP2*, *NPHP3*, and *NPHP4* (Mollet et al., 2002, 2005; Olbrich et al., 2003; Otto et al., 2003). However, a systematic connection between NPHP, JBTS, and MKS proteins has not been explored.

The proteins encoded by genes mutated in NPHP, JBTS, and MKS are found either within the primary cilium or at the basal body, and several have homologs in *Chlamydomonas* (Hildebrandt et al., 2009a), suggesting that they participate in conserved ciliary machinery. However, some of these proteins

are centrosomal even in the absence of cilia (Chang et al., 2006), suggesting that these machines may function at the centrosome, possibly to organize cell polarity or receptor trafficking, rather than simply being a structural component of the primary cilium.

To better understand the molecular mechanisms underlying NPHP-JBTS-MKS, we developed a high-confidence proteomic strategy using the G-LAP tandem-affinity method (Torres et al., 2009) to identify interactors associated with nine disease proteins. Our data show that NPHP-JBTS-MKS proteins form an interaction network that can be classified into three distinct modules: NPHP1-4-8, NPHP5-6, and Mks. Assays for ciliogenesis and epithelial morphogenesis using three-dimensional (3D) renal cultures suggest that NPHP1-4-8 links primarily to apical organization defects seen in nephronophthisis, whereas ciliary NPHP5-6 deficits appear central to retinal and potentially neural deficiency, with Mks module and Hedgehog signaling defects linked to the neural tube defects. Excitingly, our network building strategy allowed us to propose candidates for new ciliopathy disease genes, leading to the identification of the first human mutations in the NPHP gene Ataxin10 (*ATXN10*) and JBTS gene Tectonic2 (*TCTN2*).

RESULTS

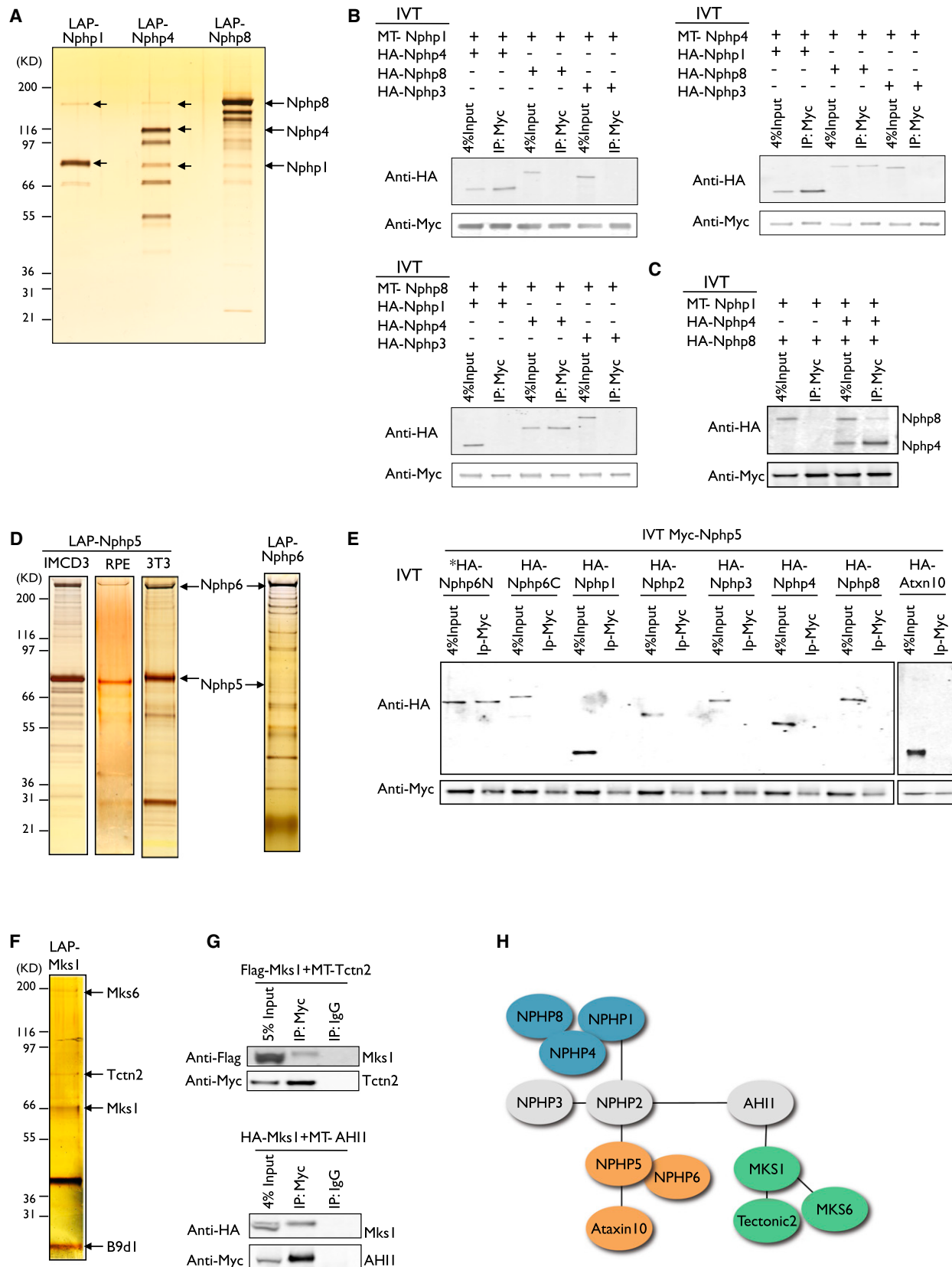
Mapping of an NPHP-JBTS-MKS Ciliopathy Protein Network

To better define physical interactions among the NPHP-JBTS-MKS disease proteins, we used the G-LAP-Flp purification strategy (Torres et al., 2009) to identify interacting proteins that copurify with the nine disease gene products known at the time that this study was initiated. The G-LAP-Flp strategy is an optimized system for rapid generation of mammalian stable cell lines that facilitates high-confidence and high-throughput proteomic studies. We created clonal Flp-In cell lines stably expressing a LAP tag (EGFP-TEV-S-peptide) fused to the amino terminus of each individual disease protein (*NPHP1*, *NPHP2/inversin*, *NPHP3*, *NPHP4*, *NPHP5/IQCB1*, *NPHP6/CEP290*, *NPHP8/RPGRIP1L*, *AHI1/Jouberin*, and *MKS1*) in NIH 3T3 fibroblasts, mouse kidney inner medullary collecting duct (IMCD3) cells, or human retinal pigment epithelial (RPE) cells. These ciliated cell models provide a physiologically relevant context for studying ciliary assembly, signaling, and cystogenesis pathways. We then isolated complexes associated with each bait protein by tandem affinity purification and identified interacting proteins by mass spectrometry (MS) (Figure S1B).

To identify bona fide interactors, we optimized the LAP purification procedure to avoid the possibility of carryover, which would severely confound the analysis of a protein network (Extended Experimental Procedures). For each candidate interactor, we evaluated metric MS data including the total number of peptides, the sum of ion currents contributing to a specific

(C–F) The NPHP-JBTS-MKS interaction network generated from the R script and visualized using Cytoscape. The entire network is shown in (C); individual subgraphs that illustrate the 1-4-8 (IMCD3), 5-6 (IMCD3), and MKS (NIH 3T3) modules are shown in (D), (E), and (F). Ellipse, protein; single-headed arrows, unreciprocated interactions (pointing to the hits); double-headed arrows (red), reciprocal interactions. Bait proteins and a subset of interactors are highlighted using the color scheme described in Figure 1B.

See also Figure S1, Figure S2, Table S1, Table S2, Table S3, Table S5, Data S1, Data S2, and Data S3.



mass spectrum (Sum TIC), and the percent sequence coverage. Data from fifteen affinity purification protein mass spectrometry (APMS) experiments were compiled into a single data set. If any single spectrum from an identifiable peptide was found, the corresponding protein was included (Table S1 and Data S1). Using the method developed by Scholtens and Gentleman (Scholtens, 2004; Scholtens et al., 2005), we performed a proteomic network analysis (Extended Experimental Procedures and Data S2), which we visualized using the Cytoscape software package (Data S3) (Shannon et al., 2003).

This method creates a ranked list of the most probable subgraphs, representing interactions (edges) between proteins (nodes) in a graphical form (Figures 1D–1F and Figure S2). Here, the nodes represent the individual NPHP, JBTS, and MKS protein baits plus the identified hits. Hits identified in an APMS experiment are hypothesized to interact with the bait protein, and this connection is represented by an edge between the bait node and the node representing the hit. If a newly identified protein (node) shows a single interaction (edge) with a bait, it is of lower informational value compared to a node that shows multiple interactions with different baits; the presence of symmetric interactions, where two baits both identify the other efficiently in the APMS experiment, is of the highest value. Here, we began our analysis by first constructing a network based solely on the physical interactions seen in our APMS data set and later incorporating additional functional data to further validate the network.

When the physical interaction data are analyzed using this method, a striking disease protein network emerges. As highlighted in Figures 1B and 1C, we find that the most significant interactors for the NPHP-JBTS-MKS disease proteins are, in fact, other disease proteins from the same group. Our data confirm some previously reported interactions, including the NPHP1-NPHP2 and NPHP1-NPHP4 interactions (Mollet et al., 2002; Otto et al., 2003). However, our analysis is more comprehensive and provides a quantitative view of the most abundant interactors (Table S1). To validate our network, we tested several newly identified interactions by coimmunoprecipitation and by in vitro binding to identify direct interactions. Our analysis reveals

that NPHP-JBTS-MKS proteins do not form a single complex but instead cluster into three biochemically distinct modules: (1) NPHP1, NPHP4, NPHP8 (“1-4-8”), (2) NPHP5, NPHP6 (“5-6”), and (3) MKS1, MKS6 (“MKS”).

Below, we describe interactions within the specific modules.

NPHP1, NPHP4, and NPHP8 Interact and Localize to Cell-Cell Contacts and the Ciliary Transition Zone

NPHP1, NPHP4, and NPHP8 show strong mutual interactions via LAP tagging. LAP-NPHP1 purifications contained endogenous NPHP4 and NPHP8 peptides in high abundance. Reciprocally, NPHP1 was identified in LAP-NPHP4 and LAP-NPHP8 purifications (Table S1 and Table S2). Visualizing purified LAP-NPHP1 on silver-stained gels revealed a substoichiometric band of NPHP8 and barely detectable NPHP4. LAP-NPHP4 purifications showed a band of NPHP8, NPHP1, and distinctive breakdown products of NPHP4. LAP-NPHP8 showed high-efficiency interactions with NPHP1 and NPHP4 (Figure 2A). Quite possibly, NPHP1-4-8 form multiple or processed complexes.

We used in vitro binding to test whether these NPHP proteins interact directly. We assayed whether in vitro-translated Myc-tagged NPHP1, NPHP4, and NPHP8 immunoprecipitate HA-tagged proteins produced by in vitro translation in wheat germ extracts. We find that NPHP4 directly binds both NPHP1 and NPHP8 in vitro and can bridge the interaction between NPHP1 and NPHP8, whereas NPHP1 and NPHP8 do not appear to bind directly (Figures 2B, 2C, and 2H).

To explore functional interactions among NPHP1, NPHP4, and NPHP8, we investigated their subcellular localization. LAP-NPHP1, LAP-NPHP4, and LAP-NPHP8 each localize diffusely in the cytoplasm of IMCD3 cells seeded at low density. Strikingly, as cells approach confluence and develop into polarized epithelial monolayers, these NPHP proteins accumulate to cell-cell contacts, mostly basolateral of tight junctions (Figure 3A and Figures S4A and S4B). The NPHP1-4-8 proteins can also be found at a specified compartment that extends between the basal body to the base of the axoneme, shown by costaining with the mother centriole marker ODF2, centriole distal appendage marker OFD1, and axonemal acetylated tubulin (Figures 3A

Figure 2. Validation of NPHP-JBTS-MKS Interactions Using Coimmunoprecipitation and In Vitro Binding Assays

(A) LAP-NPHP1, LAP-NPHP4, and LAP-NPHP8 were immunopurified from IMCD3 cells using anti-GFP antibody beads, eluted with TEV protease, and recaptured on S protein agarose. Eluates were separated on 4%–12% SDS-polyacrylamide gradient gels and were visualized by silver staining. NPHP1, NPHP4, and NPHP8 species are noted by arrows.

(B and C) NPHP4 bridges the interaction between NPHP1 and NPHP8 in vitro. Myc (MT)-tagged and HA-tagged NPHP1, NPHP4, and NPHP8 were in vitro translated using cell-free wheat germ extract. Each Myc-tagged protein was incubated with HA-tagged protein(s) and immunoprecipitated using anti-Myc beads. Eluates were separated by SDS-PAGE and immunoblotted with an anti-HA antibody. HA-NPHP3 was used as a negative control.

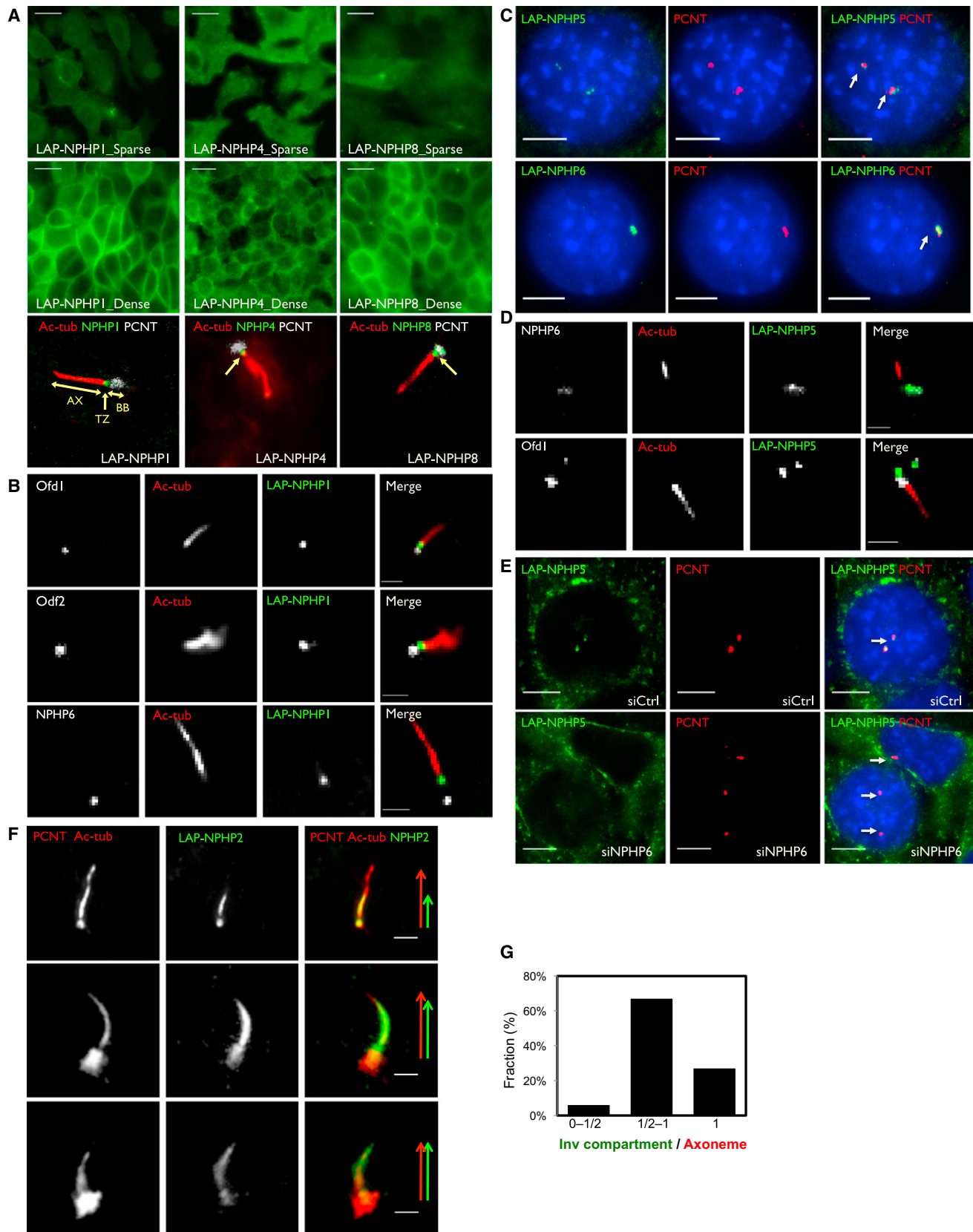
(D) LAP-NPHP5 complexes were immunopurified from IMCD3 (left), RPE (middle), and NIH 3T3 (right) cells, and LAP-NPHP6 complexes were immunopurified from IMCD3 cells as described in Figure 2A. Identified NPHP5 and NPHP6 species are noted by arrows.

(E) Interactions between NPHP5 and its associated proteins in vitro. Myc-tagged NPHP5 and HA-tagged interactors were in vitro translated and tested for direct binding using the procedure described above. NPHP5 binds directly to NPHP6 via its N-terminal domain (NPHP6N).

(F) LAP-MKS1 complexes were immunopurified from NIH 3T3 cells using the procedure described in Figure 2A. Identified MKS1, B9d1, Tctn2, and MKS6 species are noted by arrows.

(G) Validation of the interactions between MKS1 and copurified proteins Tctn2 and Ahi1. Myc-tagged Tctn2 or Ahi1 were coexpressed with Flag- or HA-tagged MKS1 in HEK293T cells and were immunoprecipitated using anti-Myc beads or control IgG beads. Eluates were separated by SDS-PAGE and immunoblotted with an anti-Flag or anti-HA antibody.

(H) Cartoon summarizing the interactions among NPHP-JBTS-MKS proteins. Ellipse, protein; black line, interaction identified by MS/MS; touching ellipses, direct interactions validated by in vitro binding. NPHP1-4-8, NPHP5-6, and MKS modules are highlighted in blue, orange, and green, respectively. See also Figure S3.



and 3B). This NPHP1-4-8 compartment is reminiscent of the ciliary transition zone, believed to function as part of the ciliary sensory machinery in worms (Fliegauf et al., 2006; Winkelbauer et al., 2005). The localization of NPHP1-4-8 at transition zones can appear even in sparse cells before the cell monolayer is fully organized into an epithelial sheet with complete adherens and apical junctions. This suggests that NPHP1-4-8 can be organized above the basal body independently from its organization at cell-cell junctions, and the basal body may be sufficient to organize the “1-4-8” compartment at the transition zone. NPHP1-4-8 each contain C2 domains, which might mediate interactions with phospholipids at cell-cell junctions or at the ciliary base.

Some previously reported interactors of NPHP1-4-8 were not seen in our purifications, including NPHP3, NPHP6, and a group of cortical regulators (Pyk2, p130Cas, PALS1, PATJ, and Par6) (Benzing et al., 2001; Delous et al., 2009; Donaldson et al., 2000; Olbrich et al., 2003; Murga-Zamalloa et al., 2010). These absences likely reflect: (1) differences in the efficiency of detecting interactions by APMS versus coimmunoprecipitation/immunoblot, (2) the difficulty of detecting membrane-protein interactions in detergent lysates, or (3) more interestingly, rewired interactions in different tissues. Notably, we did validate that NPHP1 interacts with NPHP3 by coimmunoprecipitation, showing that co-IP is more sensitive to show some interactions, compared to copurification (Figure S3D).

NPHP5 and NPHP6 Form a Complex and Localize to the Centrosome

Purifications of NPHP5 and NPHP6 consistently demonstrated strong binding between NPHP5 (MW ~68 kD) and NPHP6/CEP290 (MW ~290 kD) in NIH 3T3, IMCD3, and human RPE cells (Figure 2D, Table S1, and Table S2). We validated this interaction using *in vitro*-translated proteins and confirmed that NPHP5 binds directly to NPHP6 via an N-terminal domain spanning amino acids 1–1207, consistent with a previously published study (Schäfer et al., 2008). In mammalian cells, NPHP6 has been shown to localize to centrosomes (Chang et al., 2006). Consistently, LAP-NPHP5 and LAP-NPHP6 both colocalize with the centrosome marker pericentrin in IMCD3 cells (Figure 3C). LAP-NPHP5 also colocalizes with endogenous NPHP6, but not with the centriole-distal appendage marker ODF1 (Figure 3D). We tested whether either protein was required to recruit the other to the centrosome by siRNA depletion of

NPHP5 or NPHP6. We found that NPHP5 failed to localize to the centrosome in the absence of NPHP6 (Figure 3E). In 53% of cells, LAP-NPHP5 is fully absent from pericentrin-positive centrosomes, compared to only 9% of cells transfected with a nontargeting siRNA. Conversely, depletion of NPHP5 had no effect on NPHP6 localization (data not shown). We conclude that NPHP6 binds NPHP5 and recruits NPHP5 to the centrosome.

NPHP5 also interacts with other NPHP proteins. We observed copurification of NPHP5 with NPHP1-4-8 only in NIH 3T3 cells and with NPHP2 only in IMCD3 cells. These interactions were validated by co-IP in HEK293T cells but likely require additional proteins to bridge the interactions because NPHP5 does not bind directly to NPHP1, NPHP4, NPHP8, or NPHP2 *in vitro* (Figures 2E and 2H). In contrast to the basal body localization of NPHP5, NPHP2 was observed at the basal body but also within the primary cilium (Figure 3F). A recent study suggested that NPHP2 localized primarily to the proximal segment of the axoneme (Shiba et al., 2010), which the authors termed the “inversin compartment.” Intriguingly, we observed NPHP2/inversin compartment in a range of extensions along the axonemal structure, beginning proximally but extending distally along the axoneme (Figures 3F and 3G and Figure S4C). The distinct localizations of NPHP1-4-8, NPHP5-6, and NPHP2 suggest a hierarchy for how these interactions are organized. Further, the connections between these modules vary notably among IMCD3, RPE, and NIH 3T3 cells, suggesting that these modules may have distinct organization and functions in polarized epithelial cells not seen in fibroblasts.

NPHP5 additionally copurified with proteins previously linked to ciliogenesis. In all three cell lines, NPHP5 copurifies with Sec3; in IMCD3 cells, NPHP5 also copurified with Sec8 and Sec10 (Figure S2D). Sec3, Sec8, and Sec10 are components of the exocyst complex, a protein complex that is important in membrane trafficking and was recently shown to be required for ciliogenesis (Zuo et al., 2009). NPHP5 at the basal body may help to recruit the exocyst to a membrane compartment at the cilia base. In IMCD3 cells, we also observed copurification of NPHP5 with Ataxin 10 (Figure S2D), a protein that is linked to Spinocerebellar Ataxia, a disease with distinctive deficiencies in cerebellar signaling and function (Matsuura et al., 2000; discussed below). We validated the NPHP5-Ataxin10 interaction by co-IP, but this interaction does not appear to be direct based on *in vitro* binding (Figure S3A and Figures 2E and 2H).

Figure 3. Localization of NPHP 1-4-8, NPHP 5-6, and NPHP2 to the Ciliary Transition Zone, Centrosome, and the Inversin Compartment

- (A) IMCD3 cells stably expressing LAP-NPHP1 (green), LAP-NPHP4 (green), or LAP-NPHP8 (green) were immunostained for pericentrin (PCNT, white) and acetylated α -tubulin (ac-tub, red). AX, axoneme; TZ, transition zone; BB, basal body.
 - (B) IMCD3 cells stably expressing LAP-NPHP1 (green) were immunostained for acetylated α -tubulin (ac-tub, red) and Odf1 (white), Odf2 (white), or NPHP6 (white). (C and D) NPHP5 and NPHP6 colocalize to the centrosome.
 - (C) IMCD3 cells stably expressing LAP-NPHP5 (green) or LAP-NPHP6 (green) were immunostained for pericentrin (PCNT, red).
 - (D) IMCD3 cells stably expressing LAP-NPHP5 (green) were immunostained for acetylated α -tubulin (ac-tub, red) and NPHP6 (white) or Odf1 (white).
 - (E) Centrosomal localization of LAP-NPHP5 is disrupted upon depletion of NPHP6. IMCD3 LAP-NPHP5 (green) cells were transfected with siRNA against NPHP6 or control and then immunostained for pericentrin (PCNT, red). Nuclei were stained with Hoechst 33258 (blue).
 - (F) NPHP5-interacting protein NPHP2 localizes to the centrosome and to the cilium. IMCD3 LAP-NPHP2 cells (green) were immunostained for pericentrin (PCNT, red) and acetylated α -tubulin (ac-tub, red). Arrows exemplify variable NPHP2/inversin compartment extensions along the axoneme.
 - (G) Percentage of cilia with a range of “inversin compartment/axoneme” ratios.
- Scale bars, 10 μ m (A), 5 μ m (C and E), and 2 μ m (B, D, and F). See also Figure S4.

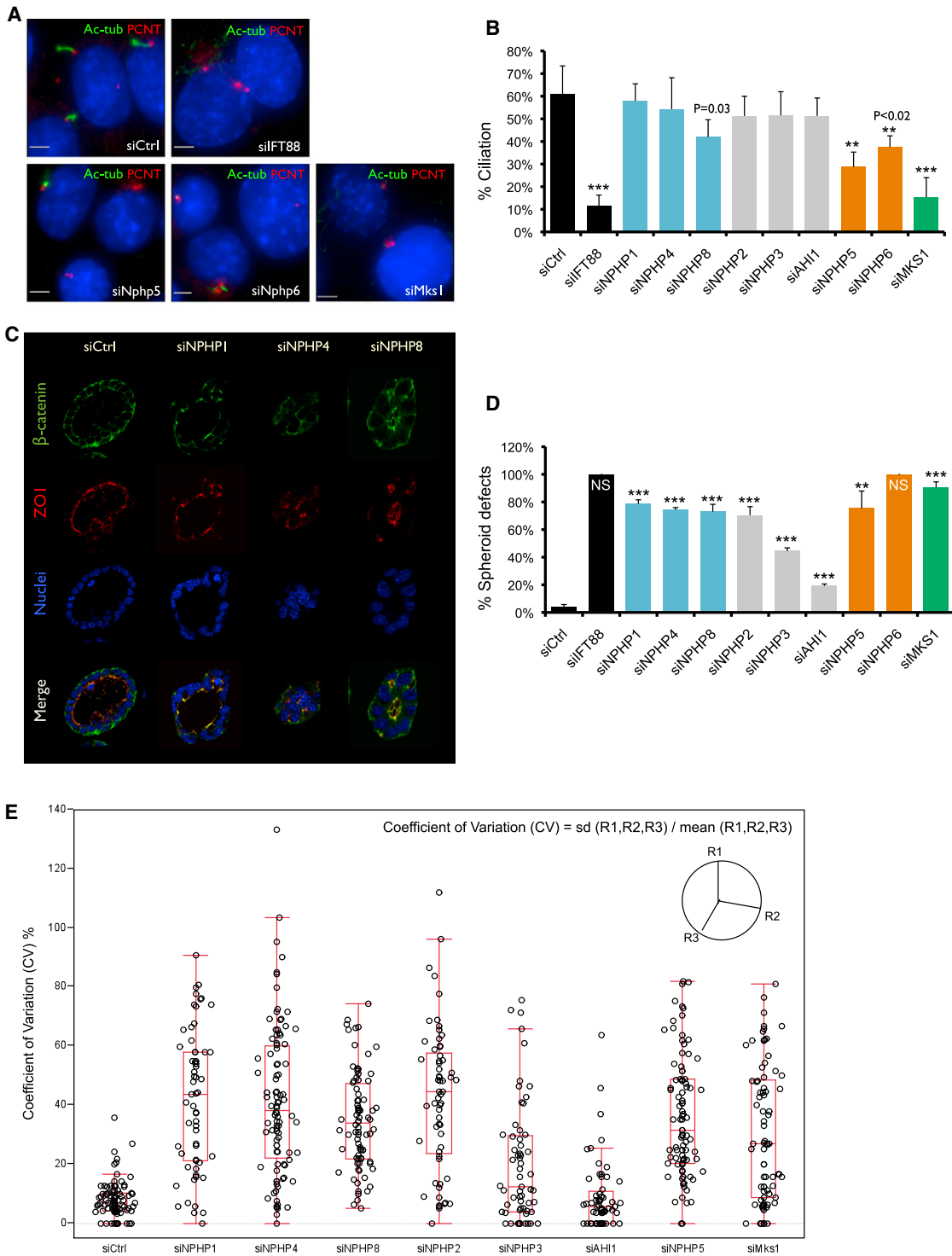


Figure 4. Functional Requirements for Ciliation and 3D Spheroid Formation Show Distinct Activities for the NPHP 1-4-8, NPHP 5-6, and MKS Modules

(A) Depletion of NPHP5, NPHP6, and MKS1 causes ciliation defects. IMCD3 cells were transfected with siRNAs against individual disease genes, IFT88, or control. Cells were fixed 72 hr posttransfection and stained for acetylated α -tubulin (green), pericentrin (red), and DNA dye Hoechst 33528 (blue). Scale bar, 5 μm . (B) Cilia were scored based on positive, adjacent staining of both pericentrin and acetylated α -tubulin. Percentage of nuclei with cilia was plotted (500–700 cells counted). Error bars represent standard error. *** $p < 0.002$; ** $p < 0.02$ (Student's t test). (C) Depletion of NPHP1, NPHP4, or NPHP8 cause spheroid defects in 3D kidney culture. IMCD3 cells were transferred to 3D collagen/Matrigel culture at 24 hr posttransfection. Spheroids were fixed 72 hr later and immunostained for β -catenin (green) and ZO1 (red). Nuclei were stained with Hoechst 33528 (blue).

Mks1 Binds to Proteins that are Important for Neural Tube Closure, Including Mks6 and Tectonic

Extending from our core interaction network in Figure 1C, we identified a third module consisting of Mks1 and its interacting proteins (Figure 1F). Mks1 localizes to the base of the cilium in vertebrates and nematodes (Bialas et al., 2009), and *MKS1* is mutated in type 1 Meckel-Gruber syndrome. Recent studies show that *Mks1* loss-of-function mouse mutant *kerouac* (*krc*) exhibits neural tube patterning defects, polydactyly, exencephaly, and biliary malformations. These are similar to the known defects in human MKS, believed to be linked to disruption of Hh signaling (Weatherbee et al., 2009). To further characterize this pathway, we purified proteins associated with Mks1 from Hh-responsive NIH 3T3 cells. Mks1 copurified with all three members of the Tectonic family of proteins (Tectonic 1–3) (Tables S1 and S2). Tectonic is a family of three potentially secreted or transmembrane proteins. Tectonic1 has been implicated in Hh-mediated patterning of the neural tube in mouse (Reiter and Skarnes, 2006), and our data suggest that Tectonic2 (*Tctn2*) is also important for Hh signaling (presented below). Other Mks1-interacting proteins include Mks6/CC2D2A (MW ~188 kD) and B9d1 (MW ~23 kD), both of which can be visualized on the silver-stained gel (Figure 2F). Mutations of *MKS6* have been identified in MKS and JBTS patients and are associated with reduced ciliogenesis and neural tube defects in these patients (Mougou-Zerelli et al., 2009; Tallila et al., 2008). B9d1, along with B9d2 and Mks1, are the three known mammalian proteins containing a B9 domain. *C. elegans* B9 proteins form a complex that localizes to the ciliary base (Williams et al., 2008). *C. elegans* B9 proteins function redundantly with nephrocystins to regulate sensory cilia morphology and behavior, whereas individual mammalian B9 protein appears to function more independently. Like Mks1, mouse B9d1 is important for Hh signal transduction (B. Chih and A. Peterson, personal communication). Therefore, Mks1 and its interactors may function as key regulators of the Hh signaling cascade to regulate proper patterning of the neural tube. Mks1, Mks6, and Tectonic1 also bind to the Joubert syndrome protein Ahi1/Joubertin, which in turn copurifies with NPHP2 (Figure 1F, Figure 2G, Figure S2B, and Table S1), suggesting Ahi1 as a potential bridging molecule.

Functional Requirements for Ciliation, 3D Spheroid Formation, and Hh Signaling Show Distinct Activities for the NPHP 1-4-8, NPHP 5-6, and MKS modules

NPHP, JBTS, and MKS are hypothesized to be diseases of ciliary dysfunction. We therefore tested whether NPHP-JBTS-MKS proteins are required for ciliogenesis. In IMCD3 cells, we found that 61% of siRNA control-treated cells formed primary cilia, as detected by staining for acetylated α -tubulin and pericentrin (Figures 4A and 4B). As a positive control, we depleted Ift88,

an intraflagellar transport component that was previously shown to be required for cilia formation (Pazour et al., 2000). As expected, depletion of Ift88 caused a dramatic decrease in ciliation (Figures 4A and 4B). We then depleted Nphp5, Nphp6, Nphp2, Nphp3, Nphp1, Nphp4, Nphp8, Ahi1, or Mks1 mRNAs by ~60%–95% using siRNAs (Figure S5B). Depletion of centrosomal proteins Nphp5 and Nphp6, along with Mks1, led to ciliogenesis defects. In contrast, normal numbers of cilia were observed in cells depleted of Nphp1, Nphp4, Nphp8, Nphp2, Nphp3, or Ahi1 (Figure 4B and Figure S5A). Our data suggest that Nphp5, Nphp6, and Mks1 are critical for ciliogenesis, whereas the other NPHP-JBTS-MKS proteins might not be strictly required for ciliogenesis under standard cell culture conditions or without much more efficient knockdown. These proteins may instead be important for establishing tissue architecture, regulating ciliary signaling or only affecting ciliogenesis in vivo.

To investigate the roles of NPHP-JBTS-MKS proteins in tissue architecture, we tested the effect of depleting these proteins in a system that reflects the cell biology of the kidney-collecting duct and thus reports on defects seen in cystic kidney diseases. Spheroid growth in 3D culture allows epithelial cells to organize into polarized, ductal structures that resemble their in vivo architecture. The spheroid systems are unique models of epithelial cell polarity and signaling (Supplemental References). Notably, IMCD3 cells are derived from collecting ducts at the cortical-medullary border, thought to be the key target cells in nephronophthisis. Using this model system, we transfected IMCD3 cells with siRNAs for Ift88, Nphp1, Nphp4, Nphp8, Nphp5, Nphp6, Nphp2, Nphp3, Ahi1, or Mks1 and then plated the transfected cells in Matrigel to induce 3D spheroid growth. After 3 days, control siRNA-treated cells formed spheroid structures with a clear lumen, apical cilia, defined tight junctions, and clear basolateral structures. Cells depleted of Ift88 or Nphp6 developed few or grossly affected spheroids, appearing as clumps of cells with few cilia evident, suggesting that ciliary genes are strongly important in spheroid formation. Consistently, depletion of Nphp5 or Mks1, genes that are required for ciliation, likewise caused spheroids to form with severe defects and few cilia evident. In striking contrast, cells depleted of Nphp1, Nphp4, Nphp8, and Nphp2 developed spheroids with irregular lumens, reduced sphericity, fewer ZO1-positive tight junctions, and perturbed localization of β -catenin (Figures 4C–4E). However, no gross abnormality of ciliogenesis was evident in these spheroids (data not shown). The apparent partition in functional requirements between ciliation and 3D spheroid formation suggests a distinct activity for the Nphp 1-4-8 module in organizing apical junctions versus the Nphp 5-6 and Mks1 modules in organizing cilia. We observed very modest disorganization of spheroids in cells depleted of Ahi1 or Nphp3 (Figures 4D and 4E), suggesting these NPHP proteins

(D) Percentage of spheroids with defects. 400–700 spheroids were counted, and error bars represent standard error. NS, no spheroids formed, shown as 100% defective. *** $p < 0.001$; ** $p < 0.01$ (Student's t test).

(E) The sphericity of a spheroid was defined using the three radii (R) measurements, which were sampled on each spheroid at 100 degree intervals. The coefficient of variation (CV) was calculated using the formula: CV = standard deviation (R1,R2,R3) / mean (R1,R2,R3). Raw CV data from each knockdown are plotted along with the outlier box plot. Lower quartile, 25th percentile; upper quartile, 75th percentile; top line, upper quartile + 1.5 \times interquartile range; bottom line, lower quartile, 1.5 \times interquartile range; middle line, 50th percentile; data points outside of the lines are outliers.

See also Figure S4, Figure S5, Table S4, Table S6, and Table S7.

may participate in mechanisms that are distinct from ciliation or apical organization.

Studies in zebrafish further supported the importance of NPHP1-4-8, 5-6, and MKS modules in apical organization and ciliary function. Knockdown of *nphp2*, *nphp5*, and *nphp6* leads to body curvature defects (Otto et al., 2003; Schäfer et al., 2008). We have also found that knockdown of additional NPHP, JBTS, and MKS proteins similarly results in body axis alterations (Figure S5D). Kupffer's vesicle (KV), the ciliated organ implicated in zebrafish left-right patterning (Essner et al., 2005), is also disrupted in these mutants (Figure S5C). The KV arises from dorsal forerunner cells (DFCs). DFCs migrate attached to the overlying surface epithelium and rearrange into rosette-like epithelial structures and then coalesce into a single rosette that differentiates into the KV with a ciliated lumen at its apical center. In addition to cilia integrity, polarity cues and apical organization are also crucial for KV morphogenesis and function (Oteíza et al., 2008), consistent with our observation that NPHP1/4/8, NPHP5, and MKS1 morphants all show KV defects.

Disruption of Hh signaling is thought to partly account for the neural tube and limb phenotypes seen in MKS patients (Weatherbee et al., 2009). MKS1 is critical for ciliogenesis, spheroid formation, and Hh signaling. However, there is no clear evidence demonstrating that NPHP5/6 are directly involved in Hh signaling. To investigate the functions of NPHP5/6 in Hh signaling, we used the standard S12 *Gli*-luciferase Hh signaling assay and observed that siRNA knockdowns of Nphp5 and Nphp6 had no effects on Hh signal transduction (Table S4). Surprisingly, ciliogenesis was also not perturbed in these cells (Table S4), suggesting that NPHP5/6 may function differently in osteoblasts (S12 cells) versus in polarized epithelial cells (IMCD3). In contrast to the requirement of MKS1 in Hh signal transduction, the specific roles of NPHP5 and NPHP6 in Hh signaling remain to be clarified.

Identification of Ataxin10 and Tectonic2 as New NPHP-JBTS Disease Proteins

Our analysis of the NPHP-JBTS-MKS network reveals extensive physical interactions among known disease proteins as well as with proteins not currently implicated in cilia-associated disorders. We reasoned that the physical interactions between specific disease proteins lead to the phenotypic overlap of these diseases and therefore hypothesized that some interacting proteins from our analysis may represent unrecognized disease loci. Remarkably, we found multiple recently reported disease proteins identified independently from our interaction network. These proteins include CC2D2A/MKS6 (Mouguo-Zerelli et al., 2009; Tallila et al., 2008), which interacts with AHI1 and MKS1, and Nek8/NPHP9, which interacts with NPHP2 (Figure 1F, Figure S2E, and Figure S3C).

With the potential to use proteomic network analysis as an unbiased means to discover new disease genes, we submitted 38 candidate genes to total genome linkage analysis to look for extensive homozygosity within candidate chromosomal intervals. This method is based on SNP analysis to predict candidate intervals that are linked to causal mutations. Genes within these intervals can then be sequenced to establish the presence of homozygous mutation. In small families lacking pedigree infor-

mation, the number of candidate intervals can be large and thus make sequencing of candidate genes impractical. Recently, a systematic approach with complete exome sequencing provided one solution to identifying specific disease alleles (Hildebrandt et al., 2009b). Here, we imagined that using our high-confidence proteomic hits would provide an enriched set to discover disease genes in NPHP/JBTS/MKS patients. Using this method, we were able to identify two new genes linked to NPHP/JBTS disease: Ataxin10 (*ATXN10*) and Tectonic2 (*TCTN2*).

First, we noted a genomic region of extensive homozygosity of 11.6 Mb on chromosome 22, with a high nonparametric linkage score for three affected siblings in a consanguineous family (A1197) from Turkey (Figure S6A). After genome analysis with 1M Affymetrix SNP chip, a homozygous *ATXN10* mutation (IVS8-3T > G) was identified in all three affected siblings. All affected children died at age 2 from kidney failure and renal biopsies, consistent with nephronophthisis (Figure 5A). One of the siblings additionally suffered from seizures and had evidence of cerebral atrophy by imaging. This mutation was absent from 90 healthy Caucasian control samples and 86 ethnically matched control individuals. We identified the protein encoded by *ATXN10*, Ataxin10, as an NPHP5-interacting protein.

Similarly, we observed a region of extensive homozygosity in a particular locus near the gene *TCTN2* in six patients with consanguineous background (Figure S6B). After sequencing all exons of *TCTN2*, a mutation was found in one family (A1443) from Turkey at IVS10-1G > A, affecting the obligatory splice acceptor site, which resulted in skipping of exon 11 (Figures 5A and 5B). The mutation was also found in a heterozygous state in the parents of a 6-year-old female who was homozygous for the mutation. She had been previously diagnosed with Joubert syndrome due to cerebellar vermis aplasia and hypotonia and had no evidence for renal disease. Again, this mutation was absent from the same control sets of Caucasian and ethnically matched healthy individuals.

With the evidence linking *TCTN2* to Joubert syndrome, we screened additional patients and identified another two Joubert families with frameshift or nonsense mutations in *TCTN2*. Patient UW95-3 had gross motor and communication delays and increased tone and reflexes, as well as bilateral talipes equinovarus deformity (clubfeet). At 15 months of age, he had no evidence of cardiovascular, renal, or liver disease by ultrasound and laboratory testing (Figure 5A). Brain MRI revealed the molar tooth sign (Figure 5C), consistent with Joubert syndrome. A homozygous mutation was identified in *TCTN2* exon 1 (c.77InsG; p.D26GfsX51) that results in frameshift and a premature stop codon (Figure S6C). Family MR20 has four affected siblings with consanguineous Pakistani background. All four patients developed childhood-onset Joubert syndrome with extremely poor learning abilities. Brain MRI revealed the molar tooth sign (Figure 5C). A homozygous nonsense mutation in *TCTN2* exon 16 (c.C1873T; p.Q625X) was identified in all four that were affected, but not in unaffected siblings (Figure 5A and Figure S6D).

Thus, from a list of 38 candidates curated by our proteomic network analysis and a modest number of patients tested, two new human disease genes were identified.

A

Gene	Family #	Origin	Nucleotide Change (State)	Deduced Protein Change	Kidney (Age at ESRF in years)	Eye	Brain	Other
ATXN10	A1197 Sib1 Sib2 Sib3	Turkey	IVS8-3T>G (homozygous)	Splice site	NPHP, Bx (2)	NAD	Seizures, mild cerebral atrophy	Died at age 2, liver fibrosis
					NPHP (2)	NAD	NAD	Liver fibrosis
					NPHP (2)	NAD	NAD	NAD
TCTN2	A1443	Turkey	IVS10-1G>A (homozygous)	Splice site	No NPHP at age 6 yr	Nystagmus	JBTS, cerebellar vermis aplasia, MTS	Muscle hypotonia
	MR20 Sib1 Sib2 Sib3 Sib4	Pakistan	c.C1873T (homozygous)	Nonsense	N/A	N/A	JBTS, MTS	N/A
	UW95-3	East Indian	c.77InsG (homozygous)	Frameshift	NAD	N/A	JBTS, MTS	NAD

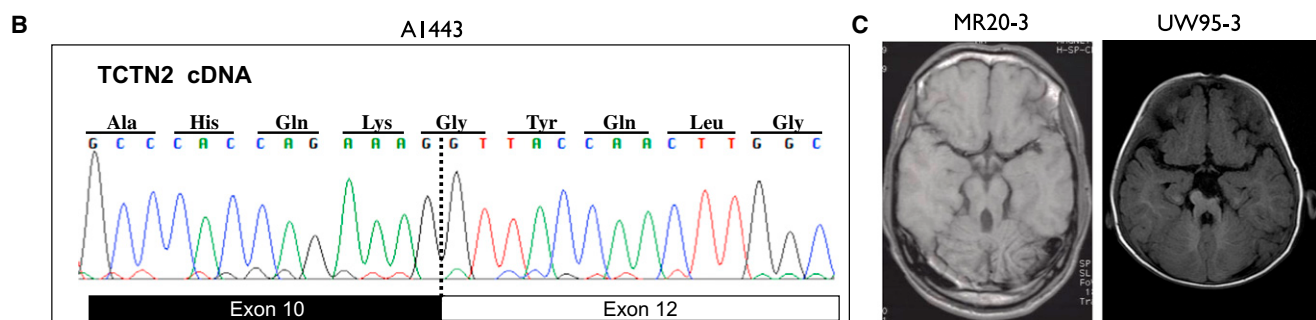


Figure 5. Identification of ATXN10 and TCTN2 as New NPHP and JBTS Disease Genes

(A) Genotype and phenotype of patients with mutations in ATXN10 and TCTN2. Bx, biopsy compatible with NPHP; MTS, molar tooth sign; NAD, nothing abnormal detected; N/A, clinical data not available.

(B) RT-PCR was performed in Joubert syndrome patient A1443 using cDNA primers to exons 7 and 14 of TCTN2. Sequencing revealed an in-frame skipping of exon 11.

(C) MRI images (T1) of Joubert syndrome patients MR20-3 and UW95-3 showing the molar tooth sign (MTS).

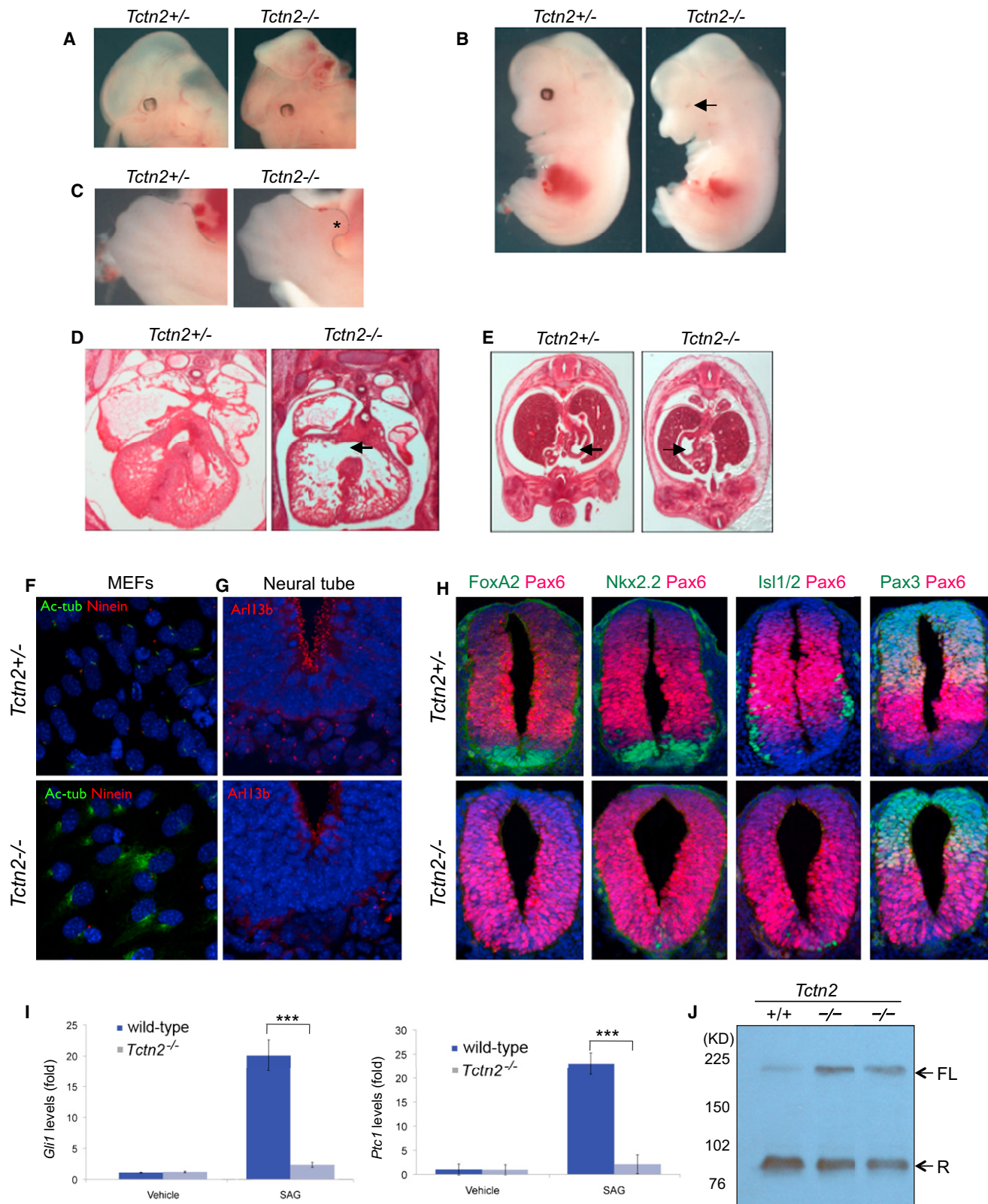
See also Figure S6.

Tctn2 Regulates Hh Signaling and Ciliogenesis

Tctn2 was identified as an interactor of Mks1, itself shown to regulate Hh-dependent neural tube patterning *in vivo* (Weatherbee et al., 2009). The human *TCTN2* mutations that we identified are associated with neural developmental defects. Based on this observation, we hypothesized that Tctn2 could be a regulator of Hh signaling. To test this hypothesis, we generated *Tctn2* null mice. On a mixed 129/Bl6 background, *Tctn2* mutants have fully penetrant neural tube closure defects, and exencephaly is apparent at E13.5 (Figure 6A). On a Bl6 background, *Tctn2*^{-/-} embryos exhibit microphthalmia, cleft palate, and polydactyly (Figures 6B and 6C), consistent with altered Hedgehog signaling. *Tctn2* mutants also have ventricular septal defects (Figure 6D) and can display right-sided stomach (Figure 6E) phenotypes characteristic of ciliary defects. To determine whether *Tctn2* is required for cilia function or formation, we examined primary cilia in mouse embryonic fibroblasts (MEFs) and neural tubes. *Tctn2* was required for ciliogenesis in isolated cells and *in vivo*, consistent with *TCTN2* being a ciliopathy gene (Figures 6F and 6G).

High-level Hh signaling is required for formation of the floor plate (Sasaki and Hogan, 1994). *Tctn2* mutants lack a morphologically distinct floor plate, and examination of FoxA2 expression in *Tctn2*^{-/-} embryos revealed that the floor plate was not specified. Similarly, Pax6, which is repressed by Hh signaling, was ventrally expanded in the absence of *Tctn2*. A severe reduction in Nkx2.2-expressing V3 interneuron progenitors and Islet1/2-expressing motor neurons further suggested defects in Hh-dependent patterning in the absence of *Tctn2* (Figure 6H).

To directly determine whether *Tctn2* is important for Hh transduction, we assayed *Ptc1* and *Gli1*, general transcriptional targets of Hh signaling, in wild-type and *Tctn2*^{-/-} MEFs. Following pathway activation by addition of a Smoothened agonist (SAG), both *Ptc1* and *Gli1* are induced ~20-fold in wild-type MEFs, whereas *Tctn2*^{-/-} MEFs display negligible responsiveness (Figure 6I). *Tctn2*^{-/-} embryos also exhibited increased amounts of full-length, unprocessed (Gli3-190) Gli3 protein (Figure 6J), indicating that *Tctn2* is important for Gli3 processing and function. Thus, *Tctn2*^{-/-} neural tubes have



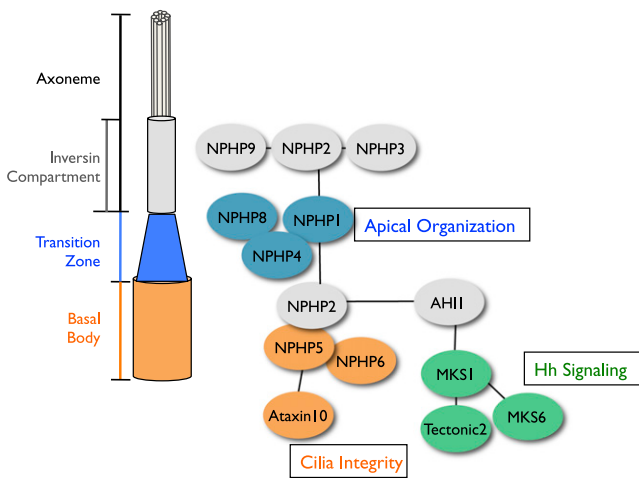


Figure 7. A Model for the NPHP-Joubert-Meckel-Gruber Network

Three interacting modules link centrosomal proteins to apical organization and to a Hedgehog regulatory network.

defects that are characteristic of altered Hh signal transduction, and *Tctn2*^{-/-} cells fail to respond to Hh agonists, suggesting that cerebellar defects in affected individuals with *TCTN2* mutations may reflect defects in ciliogenesis linked to reduced Hh signaling.

DISCUSSION

The NPHP-JBTS-MKS Interactome: A Multimodule Network Linking Ciliopathies

Using a high-confidence proteomic strategy, we have discovered and begun a systematic mapping of an NPHP-JBTS-MKS interaction network. In contrast to our earlier studies on the Bardet-Biedl syndrome (BBS) (Nachury et al., 2007), in which seven highly conserved BBS proteins formed a single, monodisperse complex, the NPHP-JBTS-MKS proteins do not form a single complex. Instead, this large group of disease proteins can be clustered into three biochemically and functionally distinct modules, in which proteins within the first two modules

show notable colocalization (Figure 7). Our studies support that genetic loss of function within each individual module drives a unique mechanism contributing to the specific histopathologic features of these disorders. The first module consists of NPHP1, NPHP4, and NPHP8, localized to cell-cell contacts and to the ciliary transition zone. They are not strongly required for ciliation, as assayed in our in vitro models. However, when kidney epithelial cells are deprived of these proteins, they form disorganized spheroids in 3D culture characterized by irregular lumens, loss of tight junctions, and perturbed localization of β -catenin. NPHP1 and NPHP4 have been reported to interact with polarity proteins PALS1, PATJ, and Par6, and depletion of NPHP1 or NPHP4 in MDCK cells results in delayed tight junction formation (Delous et al., 2009). These observations together with our data support the hypothesis that NPHP1-4-8 module organizes specialized structures at the apical surface of polarized cells and thus may participate in pathways that are important for epithelial morphogenesis and the establishment of tissue architecture. Given the effects of NPHP1-4-8 deficiency in pediatric renal disease, it will be important to examine whether this module is affected in tissues that are frequently impaired in patients with cystic kidney disease, including liver and pancreas.

Unlike the 1-4-8 module, the centrosomal module proteins NPHP5 and NPHP6 are indispensable for ciliation in IMCD3 cells; furthermore, cells fail to develop normal spheroids when depleted of NPHP5 or NPHP6, underscoring the role of centrosome/cilia integrity in tissue organization. MKS1 and its interacting proteins are grouped in the third module, characterized by their functional connection to neural tube development and Hh signal transduction.

Several of the NPHP proteins appear to bridge the three major modules, notably NPHP2 and AHI1. NPHP2, -3, and -9 interact in the inversin compartment, but the role of this new structure remains mysterious. Our preliminary data suggest that NPHP3 is particularly important for localizing specific G protein-coupled receptors (GPCRs) to the cilia (L.S. and P.K.J., unpublished data), which provides a first clue linking NPHP proteins to specific ciliary GPCR signaling pathways.

Collectively, the NPHP-JBTS-MKS interactome has provided new biochemical evidence that these disorders are highly connected and has suggested specific underlying mechanisms

Figure 6. *Tctn2* Is Required for Ciliogenesis and Hh Signaling Transduction

- (A–C) E13.5 *Tctn2*^{-/-} embryos on a mixed 129/Bl6 background have fully penetrant cranial exencephaly. On a Bl6 background, E13.5 *Tctn2*^{-/-} embryos display (B) Microphthalmia (arrow) and (C) single hindlimb preaxial polydactyly, either bilaterally or unilaterally (asterisk).
- (D and E) Hematoxylin and eosin staining of E14.5 *Tctn2*^{-/-} embryos reveals (D) ventricular septal defects (black arrow) and (E) laterality defects as evidenced by randomized stomach situs.
- (F) Mouse embryonic fibroblasts (MEFs) derived from E12.5 *Tctn2*^{+/-} embryos are ciliated, whereas *Tctn2*^{-/-} embryo-derived MEFs rarely generate cilia. Acetylated tubulin (green) marks cilia, Ninein (red) marks basal bodies and centrosomes, DAPI (blue) marks nuclei.
- (G) Immunofluorescent detection of Arl13b (red) in E9.5 transverse neural tube sections indicates that *Tctn2*^{-/-} embryos display few and abnormal cilia.
- (H) *Tctn2* is required for patterning of the ventral neural tube. Immunofluorescence of E9.5 transverse sections between the heart and hind limb stained for Pax6 in red and, in green, FoxA2, Nkx2.2, Islet1/2, or Pax3.
- (I) Levels of the Hh transcriptional targets Gli1 and Ptc1 were assessed by qPCR in MEFs derived from E12.5 *Tctn2*^{+/-} and *Tctn2*^{-/-} littermate embryos stimulated with DMSO (vehicle) or smoothened agonist (SAG) for 18 hr. *Tctn2*^{+/-} MEFs upregulate Gli1 and Ptc1 20- to 25-fold following SAG addition, whereas *Tctn2*^{-/-} MEFs are unresponsive. Experiments were performed three times in triplicate and values normalized to β -actin and presented as relative levels \pm SEM. *** $p < 0.001$ (Student's *t* test).
- (J) Lysates from E13.5 *Tctn2*^{+/-} and *Tctn2*^{-/-} littermate embryos immunoblotted for Gli3. In wild-type embryos, the majority of Gli3 is processed into a truncated repressor form (R). *Tctn2* mutants have increased levels of unprocessed full-length (FL) Gli3.

See also Figure S7.

leading to disease progression. Our 3D culture system appears to effectively mirror requirements for genes that suppress cystic kidney disease, including those that function to organize apical structures in the cell, notably NPHP1-4-8. For other genes such as NPHP5, NPHP6, and Mks1, broader defects in centrosome/cilia integrity and ciliary signaling may lead to tissue failure not only in the kidney, but also in a variety of other organs, including the neural tube and eye. Therefore, to our understanding, not all of the “ciliopathies” are simply caused by the absence of cilia per se. They rather represent a manifestation of defects in multiple interlinked cellular mechanisms. More intriguingly, whereas mild renal cysts may arise simply as a result of tissue organization defect, lack of centrosome/cilia integrity would generally predict more severe phenotypes, notably retinal degeneration; ciliary disruption with altered Hh signaling appears linked to cerebellar malformation and neural tube defects.

The NPHP-JBTS-MKS Network Is Distinct from BBSome and IFT Complexes

Bardet-Biedl syndrome (BBS) shares a number of common phenotypes with NPHP, JBTS, and MKS, including kidney cysts, retinal degeneration, polydactyly, and mental retardation. There is a single documented BBS family with mutations in each of *MKS1/BBS13* and *NPHP6/BBS14*, suggesting, at a minimum, a genetic interaction between BBS and MKS (reviewed by [Zaghoul and Katsanis, 2009](#)). However, we did not observe notable physical interactions between the NPHP-JBTS-MKS network and components of BBSome, other BBS proteins, or more than 14 BBS1-interacting proteins (C. Westlake and P.K.J., unpublished data). A reasonable hypothesis is that the shared phenotypes are likely due to broader disruption of some key regulatory pathways, such as the Hh signaling, Wnt signaling, cell polarity, or centrosome control of the cytoskeleton.

We also evaluated whether the NPHP-JBTS-MKS network proteins link to intraflagellar transport (IFT). The IFT process is essential for the formation of cilia, and defects in IFT may lead to cystic kidney disease and retinal degeneration ([Davenport et al., 2007](#); [Rosenbaum and Witman, 2002](#)). Interestingly, NPHP-JBTS-MKS network also does not overlap with components of IFT-A or IFT-B complex proteins (S. Mukhopadhyay and P.K.J., unpublished data), with the notable exception of an interaction between NPHP5 and IFT122 ([Table S1](#)). A recent publication suggests that *Chlamydomonas* NPHP6/CEP290 is a transition zone protein that is important for tethering flagellar membrane to the transition zone, and loss of NPHP6/CEP290 results in an imbalance of IFT complexes in the flagellum ([Craige et al., 2010](#)). This is consistent with our model that NPHP proteins participate in a mechanism anchoring the transition zone to the centrosome and cell cortex. It will be intriguing to determine whether any of the mammalian transition zone proteins (such as NPHP1, 4, and 8) or centrosomal proteins NPHP5/6 functionally link to IFT.

High-Confidence Proteomic Analysis Accelerates Discovery of New Disease Genes

The identification of an NPHP-JBTS-MKS network not only linked human genetics with underlying cellular mechanisms, but also accelerated the discovery of new NPHP-JBTS disease

genes. The causative genes are still unknown in ~70% of patients with NPHP ([Hildebrandt et al., 2009a](#)). Employing protein interaction data to predict new candidate genes involved in human genetic disorders has been explored ([Lim et al., 2006](#); [Goh et al., 2007](#); [Supplemental References](#)). However, lack of orthogonal information remains a major challenge in discovering new disease genes ([Sowa et al., 2009](#)). Our proteomic strategy has proved to be a highly effective approach, confirming two new disease loci among 38 candidate genes that were suggested by our network.

A pentanucleotide expansion of *ATXN10* results in Spinocerebellar ataxia type 10, a neurodegenerative disease involving cerebellar dysfunction leading to ataxia and seizures ([Matsuura et al., 2000](#)). Additionally, Atxn10 has a proposed role in cerebellar neuron survival and neuritogenesis through an interaction with G protein $\beta 2$ subunit ([Waragai et al., 2006](#)). Depletion of Atxn10 in 3D kidney culture leads to modest defects in both spheroid organization and ciliogenesis ([Figures S6E and S6F](#)). We hypothesize that these defects may directly contribute to the kidney phenotypes observed in the NPHP patients. Further investigation will help to clarify the various functions of Atxn10 in Nephronophthisis and in Spinocerebellar ataxia.

Tctn2 is a member of the Tectonic family proteins ([Reiter and Skarnes, 2006](#)) and, similar to *Tctn1*, is important for Hh signal transduction. Intriguingly, whereas *Tctn2* is indispensable for ciliogenesis in the neural tube, knockdown of *Tctn2* in kidney IMCD3 cells only causes modest ciliation and spheroid defects ([Figures S6E and S6F](#)). Such distinct requirements may reflect differences in expression profiles as well as the complexity of the organs involved. Indeed, *Tctn2* is highly expressed in embryonic brain tissues but below the limit of detection in the kidney ([Figure S6G](#)). The tissue distribution pattern of *Tctn2* and the differences in requirements for ciliogenesis are consistent with the *TCTN2* patient phenotypes, which show cerebellar vermis aplasia but no renal disease.

Included in our NPHP-JBTS-MKS network are numerous new interacting proteins. Many of those proteins are functioning in fundamental cellular processes, such as cytoskeletal organization, intracellular transport, and enzymatic reactions ([Table S3](#)). Therefore, the NPHP-JBTS-MKS network has provided a road-map not only for discovering new ciliopathy genes, but also for unveiling novel disease pathways. Moreover, because cell polarity and ciliary signaling defects have been implicated in a number of other diseases, notably cancer, the NPHP-JBTS-MKS network may also help to advance our understanding of cancer and suggest potential therapeutic targets.

EXPERIMENTAL PROCEDURES

Proteomic Network Analysis

Data from 15 affinity purification protein mass spectrometry experiments were compiled into a single data set. If any single spectrum from an identifiable peptide was found, the corresponding protein was included. Of the resulting 850 unique hits, 12 proteins under current investigation were excluded from the data set; all protein identifiers were mapped to Ensemble Gene IDs and to common gene names. This data set is available as the tab-delimited file [Data S1](#) in the [Supplemental Information](#). Further processing reduced this data set to one comprising the results of the 3T3 and IMCD3 experiments only and removed proteins that are either annotated to the “Keratin filament”

term in the GO Cellular Component Ontology or that include “keratin” in the gene name. The complete peptide and scoring information is available in Table S5. An adjacency matrix was compiled for each cell line experiment, and from these matrices, we derived two interaction networks. Each network’s maximal bait-hit complete subgraphs were found and were merged using sensitivity and specificity parameters of 0.7 and 0.75, respectively (Scholtens et al., 2005). These resulting estimates of protein complex composition were plotted from within R, and the entire networks were exported for display in Cytoscape (Shannon et al., 2003). Enrichment of each network and its inferred subcomplexes for GO terms was assessed using Fisher’s exact test, with the universe of genes defined as the set of mouse Ensemble Gene IDs having GO term annotations. Although this test does not explicitly account for correlation of GO term enrichment due to the ontologies’ graph structures, it serves to provide a general view of the processes, functions, and locations of the networks and their subgraphs. All data set manipulations and subsequent analyses were performed using R version 2.11.1. Analysis of subgraphs used the package “apComplex” version 2.14.0 (Scholtens, 2004), and gene set enrichment analysis for GO terms used “topGO” version 1.16.2. The analysis script and session information are included in Data S2 in the Supplemental Information.

SUPPLEMENTAL INFORMATION

Supplemental Information includes Extended Experimental Procedures, seven figures, seven tables, and three data files and can be found with this article online at doi:10.1016/j.cell.2011.04.019.

ACKNOWLEDGMENTS

The authors acknowledge expert advice and contributions from Chris Westlake, Guowei Fang, Ben Chih, Andy Peterson, Cecile Chalouni, John S. Beck, Darryl Y. Nishimura, Charles C. Searby, Martin Griebel, John Neveu, Bogdan Budnik, Renee Robinson, Alex Loktev, Jorge Torres, Saikat Mukhopadhyay, Dirk Siepe, and Kevin Wright. We acknowledge the following support: J.J.M., NIH Medical Scientist Training Program Grant GM07365-33; R.H.G., the Netherlands Organisation for Scientific Research VIDI grant 016.066.354 and the EU FP7 “Syscilia” project 241955; L.M.B., the Cardiovascular Center Interdisciplinary Research Fellowship, University of Iowa; J.F.O., NIH grant DK071108; D.C.S., NIH Grant CA112369; J.B.V., Canadian Institutes of Health Research grant MOP-102758; D.A.D., KL2RR025015 and R01NS064077; J.F.R., NIH Grant R01-AR054396, the March of Dimes, the Burroughs Wellcome Fund, the Packard Foundation, and the Sandler Family Supporting Foundation; V.C.S., NIH Grants R01-EY11298, R01-EY017168, the Roy J. Carver Charitable Trust, Carver Endowment for Molecular Ophthalmology, and Research to Prevent Blindness. V.C.S. is an HHMI investigator. F.H. is an HHMI Investigator, a Doris Duke Distinguished Clinical Scientist, and a Frederick G.L. Huetwell Professor. F.H. acknowledges support from the NIH grants (DK1068306, DK1069274, and DK090917). L.S., M.J.B., X.W., S.J.S., M.K., E.G.H., M.K.S., W.S., J.F.B., P.K., and P.K.J. are employees of Genentech, Inc.

Received: October 1, 2010

Revised: March 16, 2011

Accepted: April 27, 2011

Published: May 12, 2011

REFERENCES

- Baala, L., Audollent, S., Martinovic, J., Ozilou, C., Babron, M.C., Sivanandamoorthy, S., Saunier, S., Salomon, R., Gonzales, M., Rattenberry, E., et al. (2007). Pleiotropic effects of CEP290 (NPHP6) mutations extend to Meckel syndrome. *Am. J. Hum. Genet.* 81, 170–179.
- Benzing, T., Gerke, P., Höpker, K., Hildebrandt, F., Kim, E., and Walz, G. (2001). Nephrocystin interacts with Pyk2, p130(Cas), and tensin and triggers phosphorylation of Pyk2. *Proc. Natl. Acad. Sci. USA* 98, 9784–9789.
- Bialas, N.J., Inglis, P.N., Li, C., Robinson, J.F., Parker, J.D., Healey, M.P., Davis, E.E., Inglis, C.D., Toivonen, T., Cottell, D.C., et al. (2009). Functional interactions between the ciliopathy-associated Meckel syndrome 1 (MKS1) protein and two novel MKS1-related (MKS1) proteins. *J. Cell Sci.* 122, 611–624.
- Chang, B., Khanna, H., Hawes, N., Jimeno, D., He, S., Lillo, C., Parapuram, S.K., Cheng, H., Scott, A., Hurd, R.E., et al. (2006). In-frame deletion in a novel centrosomal/ciliary protein CEP290/NPHP6 perturbs its interaction with RPGR and results in early-onset retinal degeneration in the rd16 mouse. *Hum. Mol. Genet.* 15, 1847–1857.
- Corbit, K.C., Aanstad, P., Singla, V., Norman, A.R., Stainier, D.Y., and Reiter, J.F. (2005). Vertebrate Smoothened functions at the primary cilium. *Nature* 437, 1018–1021.
- Craigie, B., Tsao, C.C., Diener, D.R., Hou, Y., Lechtreck, K.F., Rosenbaum, J.L., and Witman, G.B. (2010). CEP290 tethers flagellar transition zone microtubules to the membrane and regulates flagellar protein content. *J. Cell Biol.* 190, 927–940.
- Davenport, J.R., Watts, A.J., Roper, V.C., Croyle, M.J., van Groen, T., Wyss, J.M., Nagy, T.R., Kesterson, R.A., and Yoder, B.K. (2007). Disruption of intraflagellar transport in adult mice leads to obesity and slow-onset cystic kidney disease. *Curr. Biol.* 17, 1586–1594.
- Delous, M., Hellman, N.E., Gaudé, H.M., Silbermann, F., Le Bivic, A., Salomon, R., Antignac, C., and Saunier, S. (2009). Nephrocystin-1 and nephrocystin-4 are required for epithelial morphogenesis and associate with PALS1/PATJ and Par6. *Hum. Mol. Genet.* 18, 4711–4723.
- Donaldson, J.C., Dempsey, P.J., Reddy, S., Bouton, A.H., Coffey, R.J., and Hanks, S.K. (2000). Crk-associated substrate p130(Cas) interacts with nephrocystin and both proteins localize to cell-cell contacts of polarized epithelial cells. *Exp. Cell Res.* 256, 168–178.
- Essner, J.J., Amack, J.D., Nyholm, M.K., Harris, E.B., and Yost, H.J. (2005). Kupffer’s vesicle is a ciliated organ of asymmetry in the zebrafish embryo that initiates left-right development of the brain, heart and gut. *Development* 132, 1247–1260.
- Fliegauf, M., Horvath, J., von Schnakenburg, C., Olbrich, H., Müller, D., Thumfarth, J., Schermer, B., Pazour, G.J., Neumann, H.P., Zentgraf, H., et al. (2006). Nephrocystin specifically localizes to the transition zone of renal and respiratory cilia and photoreceptor connecting cilia. *J. Am. Soc. Nephrol.* 17, 2424–2433.
- Goh, K.I., Cusick, M.E., Valle, D., Childs, B., Vidal, M., and Barabási, A.L. (2007). The human disease network. *Proc. Natl. Acad. Sci. USA* 104, 8685–8690.
- Hildebrandt, F., Attanasio, M., and Otto, E. (2009a). Nephronophthisis: disease mechanisms of a ciliopathy. *J. Am. Soc. Nephrol.* 20, 23–35.
- Hildebrandt, F., Heeringa, S.F., Rüschendorf, F., Attanasio, M., Nürnberg, G., Becker, C., Seelow, D., Huebner, N., Chernin, G., Vlangos, C.N., et al. (2009b). A systematic approach to mapping recessive disease genes in individuals from outbred populations. *PLoS Genet.* 5, e1000353.
- Huangfu, D., Liu, A., Rakeman, A.S., Murcia, N.S., Niswander, L., and Anderson, K.V. (2003). Hedgehog signalling in the mouse requires intraflagellar transport proteins. *Nature* 426, 83–87.
- Lee, J.H., and Gleeson, J.G. (2010). The role of primary cilia in neuronal function. *Neurobiol. Dis.* 38, 167–172.
- Lim, J., Hao, T., Shaw, C., Patel, A.J., Szabó, G., Rual, J.F., Fisk, C.J., Li, N., Smolyar, A., Hill, D.E., et al. (2006). A protein-protein interaction network for human inherited ataxias and disorders of Purkinje cell degeneration. *Cell* 125, 801–814.
- Matsuura, T., Yamagata, T., Burgess, D.L., Rasmussen, A., Grewal, R.P., Watase, K., Khajavi, M., McCall, A.E., Davis, C.F., Zu, L., et al. (2000). Large expansion of the ATTCT pentanucleotide repeat in spinocerebellar atrophy type 10. *Nat. Genet.* 26, 191–194.
- Mollet, G., Salomon, R., Gribouval, O., Silbermann, F., Bacq, D., Landthaler, G., Milford, D., Nayir, A., Rizzoni, G., Antignac, C., and Saunier, S. (2002). The gene mutated in juvenile nephronophthisis type 4 encodes a novel protein that interacts with nephrocystin. *Nat. Genet.* 32, 300–305.

- Mollet, G., Silbermann, F., Delous, M., Salomon, R., Antignac, C., and Saunier, S. (2005). Characterization of the nephrocystin/nephrocystin-4 complex and subcellular localization of nephrocystin-4 to primary cilia and centrosomes. *Hum. Mol. Genet.* 14, 645–656.
- Mouguo-Zerelli, S., Thomas, S., Szenker, E., Audollent, S., Elkhartoufi, N., Babarit, C., Romano, S., Salomon, R., Amiel, J., Esculpavit, C., et al. (2009). CC2D2A mutations in Meckel and Joubert syndromes indicate a genotype-phenotype correlation. *Hum. Mutat.* 30, 1574–1582.
- Murga-Zamalloa, C.A., Desai, N.J., Hildebrandt, F., and Khanna, H. (2010). Interaction of ciliary disease protein retinitis pigmentosa GTPase regulator with nephronophthisis-associated proteins in mammalian retinas. *Mol. Vis.* 16, 1373–1381.
- Nachury, M.V., Loktev, A.V., Zhang, Q., Westlake, C.J., Peränen, J., Merdes, A., Slusarski, D.C., Scheller, R.H., Bazan, J.F., Sheffield, V.C., and Jackson, P.K. (2007). A core complex of BBS proteins cooperates with the GTPase Rab8 to promote ciliary membrane biogenesis. *Cell* 129, 1201–1213.
- Olbrich, H., Fliegauf, M., Hoefele, J., Kispert, A., Otto, E., Volz, A., Wolf, M.T., Sasmaz, G., Trauer, U., Reinhardt, R., et al. (2003). Mutations in a novel gene, NPHP3, cause adolescent nephronophthisis, tapeto-retinal degeneration and hepatic fibrosis. *Nat. Genet.* 34, 455–459.
- Otto, E.A., Schermer, B., Obara, T., O'Toole, J.F., Hiller, K.S., Mueller, A.M., Ruf, R.G., Hoefele, J., Beekmann, F., Landau, D., et al. (2003). Mutations in INVS encoding inversin cause nephronophthisis type 2, linking renal cystic disease to the function of primary cilia and left-right axis determination. *Nat. Genet.* 34, 413–420.
- Oteiza, P., Köppen, M., Concha, M.L., and Heisenberg, C.P. (2008). Origin and shaping of the laterality organ in zebrafish. *Development* 135, 2807–2813.
- Parisi, M.A., Doherty, D., Chance, P.F., and Glass, I.A. (2007). Joubert syndrome (and related disorders) (OMIM 213300). *Eur. J. Hum. Genet.* 15, 511–521.
- Pazour, G.J., Dickert, B.L., Vucica, Y., Seeley, E.S., Rosenbaum, J.L., Witman, G.B., and Cole, D.G. (2000). Chlamydomonas IFT88 and its mouse homologue, polycystic kidney disease gene tg737, are required for assembly of cilia and flagella. *J. Cell Biol.* 151, 709–718.
- Reiter, J.F., and Skarnes, W.C. (2006). Tectonic, a novel regulator of the Hedgehog pathway required for both activation and inhibition. *Genes Dev.* 20, 22–27.
- Rosenbaum, J.L., and Witman, G.B. (2002). Intraflagellar transport. *Nat. Rev. Mol. Cell Biol.* 3, 813–825.
- Salonen, R., and Paavola, P. (1998). Meckel syndrome. *J. Med. Genet.* 35, 497–501.
- Sasaki, H., and Hogan, B.L. (1994). HNF-3 beta as a regulator of floor plate development. *Cell* 76, 103–115.
- Schäfer, T., Pütz, M., Lienkamp, S., Ganner, A., Bergbreiter, A., Ramachandran, H., Gieloff, V., Gerner, M., Mattonet, C., Czarnecki, P.G., et al. (2008). Genetic and physical interaction between the NPHP5 and NPHP6 gene products. *Hum. Mol. Genet.* 17, 3655–3662.
- Shannon, P., Markiel, A., Ozier, O., Baliga, N.S., Wang, J.T., Ramage, D., Amin, N., Schwikowski, B., and Ideker, T. (2003). Cytoscape: a software environment for integrated models of biomolecular interaction networks. *Genome Res.* 13, 2498–2504.
- Scholtens, D. (2004). apComplex: Estimate protein complex membership using AP-MS protein data. R package version 2.14.0.
- Scholtens, D., Vidal, M., and Gentleman, R. (2005). Local modeling of global interactome networks. *Bioinformatics* 21, 3548–3557.
- Shiba, D., Manning, D.K., Koga, H., Beier, D.R., and Yokoyama, T. (2010). Inv acts as a molecular anchor for Nphp3 and Nek8 in the proximal segment of primary cilia. *Cytoskeleton (Hoboken)* 67, 112–119.
- Sowa, M.E., Bennett, E.J., Gygi, S.P., and Harper, J.W. (2009). Defining the human deubiquitinating enzyme interaction landscape. *Cell* 138, 389–403.
- Tallila, J., Jakkula, E., Peltonen, L., Salonen, R., and Kestilä, M. (2008). Identification of CC2D2A as a Meckel syndrome gene adds an important piece to the ciliopathy puzzle. *Am. J. Hum. Genet.* 82, 1361–1367.
- Torres, J.Z., Miller, J.J., and Jackson, P.K. (2009). High-throughput generation of tagged stable cell lines for proteomic analysis. *Proteomics* 9, 2888–2891.
- Waragai, M., Nagamitsu, S., Xu, W., Li, Y.J., Lin, X., and Ashizawa, T. (2006). Ataxin 10 induces neurogenesis via interaction with G-protein beta2 subunit. *J. Neurosci. Res.* 83, 1170–1178.
- Weatherbee, S.D., Niswander, L.A., and Anderson, K.V. (2009). A mouse model for Meckel syndrome reveals Mks1 is required for ciliogenesis and Hedgehog signaling. *Hum. Mol. Genet.* 18, 4565–4575.
- Williams, C.L., Winkelbauer, M.E., Schafer, J.C., Michaud, E.J., and Yoder, B.K. (2008). Functional redundancy of the B9 proteins and nephrocystins in *Caenorhabditis elegans* ciliogenesis. *Mol. Biol. Cell* 19, 2154–2168.
- Winkelbauer, M.E., Schafer, J.C., Haycraft, C.J., Swoboda, P., and Yoder, B.K. (2005). The *C. elegans* homologs of nephrocystin-1 and nephrocystin-4 are cilia transition zone proteins involved in chemosensory perception. *J. Cell Sci.* 118, 5575–5587.
- Zaghoul, N.A., and Katsanis, N. (2009). Mechanistic insights into Bardet-Biedl syndrome, a model ciliopathy. *J. Clin. Invest.* 119, 428–437.
- Zuo, X., Guo, W., and Lipschutz, J.H. (2009). The exocyst protein Sec10 is necessary for primary ciliogenesis and cystogenesis in vitro. *Mol. Biol. Cell* 20, 2522–2529.

Supplemental Information

EXTENDED EXPERIMENTAL PROCEDURES

Clones and Plasmids

Mouse disease gene cDNAs were synthesized by DNA 2.0 into Gateway compatible pDONR221 entry vectors and inserted into appropriate Gateway destination vectors using LR recombination (Invitrogen). pCS2+Myc_DEST and pCS2+HA_DEST, used for mammalian expression, were created by inserting a Gateway recombination reading frame cassette into the StuI site in pCS2+Myc, or pCS2+HA. For stable cell line creation, cystoprotein genes were inserted into pG-LAP1 and pG-LAP3 vectors created previously by our laboratory (Torres et al., 2009) and available at Addgene.org.

Generation of G-Lap-Flp Cell Lines

The NIH 3T3 Flp-In cell line was obtained from Invitrogen. IMCD3 and RPE cell lines were obtained from ATCC and converted to an Flp-In cell line by the insertion of an FRT site. Stable cell lines were created as previously described (Torres et al., 2009). Briefly, pG-LAP construct encoding protein of interest was cotransfected with pOG44 (Invitrogen) into Flp-In cell lines using Fugene 6 (Roche) and selected for stable integrants using Hygromycin B or Puromycin.

Tandem Affinity Purification and Mass Spectrometry

To best optimize the LAP purification procedure and minimize the possibility of carryover, we have standardized the growth of cells, the preparation of extracts, and the method of tandem affinity purification (Torres et al., 2009). Briefly, stable LAP cell lines were harvested using detergent. Lysates were clarified at 43,000 rpm and subjected to anti-GFP immunoprecipitation. Bound proteins were eluted from antibody beads using TEV protease, recaptured on S-protein agarose (Novagen), and eluted in 4x NuPAGE sample buffer (Invitrogen). Following purification, great care is taken to ensure a lack of contamination from both environmental sources and from other purified proteins. Each purified set of interacting proteins is separated on an individual 10% Bis-Tris polyacrylamide gel and stained with Coomassie brilliant blue. NIH 3T3 samples and RPE samples were run into gels ~10mm, and gel slices were further divided into 10 x1 mm slices. IMCD3 samples were run into gels for 20–40mm and divided into 20–40 x1 mm slices. Each excised lane was, reduced, carboxyamidomethylated and digested with trypsin. Peptide identification of each digestion mixture was performed by microcapillary reversed-phase HPLC nanoelectrospray tandem mass spectrometry (μ LC-MS/MS) on an LTQ-Orbitrap Velos or XL mass spectrometer (ThermoFisher Scientific, San Jose, MA). The Orbitrap repetitively surveyed an *m/z* range from 395 to 1600, while data-dependent MS/MS spectra on the twenty (Velos) or ten (XL) most abundant ions in each survey scan were acquired in the linear ion trap. MS/MS spectra were acquired with relative collision energy of 30%, 2.5-Da isolation width, and recurring ions dynamically excluded for 60 s. Preliminary sequencing of peptides was facilitated with the SEQUEST algorithm with a 30 ppm mass tolerance against a species specific (mouse or human) subset of the UniProt Knowledgebase. With a custom version of the Harvard Proteomics Browser Suite (ThermoFisher Scientific, San Jose CA), peptide spectrum matches (PSMs) were accepted with mass error < 2.5ppm and score thresholds to attain an estimated false discovery rate (FDR) of ~1% using a reverse decoy database strategy. For IMCD3-LAP-GFP ctrl and IMCD3-LAP-NPHP4 samples, peptide identification was performed using NanoAcuity UPLC (Waters Corp, Milford, MA). Samples were analyzed on-line via nanospray ionization into a hybrid LTQ-Orbitrap mass spectrometer (Thermo Scientific, San Jose, CA). Data were collected in data dependent mode with the parent ion being analyzed in the FTMS and the top 8 most abundant ions being selected for fragmentation and analysis in the LTQ. Tandem mass spectrometric data were analyzed using the Mascot search algorithm (Matrix Sciences, London, UK) against the mouse Uniprot database (including reverse hits and contaminants) and filtered to a 5% FDR.

Generation of the Networks and Figures

Data

The dataset is contained in the tab-delimited text file [Data S1](#). Each row represents a protein identified in one of the LAP-tag APMS experiments. Columns are: (1) Name of original report file; (2) Cell line; (3) Bait protein name; (4) Hit protein identifier (in the format provided by the MS lab); (5) Ensembl gene identifier (“Stable ID”) corresponding to the bait protein; (6) Ensembl gene identifier for the hit protein (7) Gene name for the bait protein; (8) Gene name for the hit protein; (9) Total Ion Current (TIC): Not available for all experiments and not used in this analysis; (10) Number of spectra (total peptides).

Script

The R script for processing the data, finding the subgraphs, printing the network diagrams and exporting the results to Cytoscape-readable format is in the text file [Data S2](#). The script loads the necessary packages (apComplex, topGO and biomaRt) and defines two functions for subsequent use. It then loads and filters the data, finds and outputs GO annotation results, and finds and prints to pdf files the subgraphs in each of the 3T3 and IMCD3 networks. All packages are available via Bioconductor (<http://www.bioconductor.org>). Various permutations of the R engine may be freely downloaded from the R-project site (<http://www.r-project.org>).

Using the Script

Assuming that the necessary packages are loaded, the script can be sourced from within R and will automatically generate files containing the results. While the GO analysis will be completed by this script, output has been turned off. To get a graph or table of significant GO nodes, uncomment the relevant lines in the ‘visualize GO results’ section of the script. The script uses a few default

parameters that may be modified and re-run. First, the threshold for a protein's inclusion in the analysis is that at least one peptide spectrum was identified from that protein. This parameter ('peptide.cutoff') may be increased to examine the effect of more stringent inclusion criteria. Second, proteins were excluded if they were annotated to the 'Keratin filament' GO term, or if the gene name was labeled as keratin. Other exclusion criteria may be added to the script, including those that make use of some of the negative control experiments in the data set. Finally, the default values of the sensitivity and specificity parameters of apComplex were used, and may be changed in the script. For further information see the documentation for the packages apComplex and topGO.

Output Files

Automatically generated output from the script includes the following files: (1) 3T3.subgraphs.pdf and IMCD3.subgraphs.pdf: network diagrams showing the Multi-Bait, Multi-Edge (MBME), Single Bait, Multi-Hits (SBMH) and Unreciprocated Bait-Bait (UnRBB) subgraphs in each network; (2) 3T3.sif and IMCD3.sif: network definition files for import into Cytoscape; (3) 3T3 and IMCD3 node attribute files ('.noa' extension): node attributes, including bait protein identity and subgraph membership for each network.

Visualizing the Networks

The .sif and .noa files may be imported into Cytoscape for visualization. We have already done this for both networks, and saved the resulting session file as [Data S3](#). From within Cytoscape a wide variety of layouts and labeling schemes may be applied to the networks. Cytoscape is freely available at <http://www.cytoscape.org>.

Session Information

The following packages and parameter settings were loaded for this analysis: (1) R version 2.11.1 (2010-05-31), x86_64-unknown-linux-gnu; (2) Locale: LC_CTYPE = en_US.UTF-8, LC_NUMERIC = C, LC_TIME = en_US.UTF-8, LC_COLLATE = en_US.UTF-8, LC_MONETARY = C, LC_MESSAGES = en_US.UTF-8, LC_PAPER = en_US.UTF-8, LC_NAME = C, LC_ADDRESS = C, LC_TELEPHONE = C, LC_MEASUREMENT = en_US.UTF-8, LC_IDENTIFICATION = C; (3) Base packages: grid, stats, graphics, utils, datasets, grDevices, methods, base; (4) Other packages: Rgraphviz_1.26.0, topGO_1.16.2, SparseM_0.85, GO.db_2.4.1, AnnotationDbi_1.10.2, Biobase_2.8.0, biomaRt_2.4.0, apComplex_2.14.0, RSQLite_0.9-2, DBI_0.2-5, RBGL_1.24.0, graph_1.26.0, gneconfig_1.0; (5) Loaded via a namespace (and not attached): lattice_0.18-8, org.Sc.sgd.db_2.4.1, RCurl_1.4-3, tools_2.11.1, XML_3.1-0.

In Vitro Translation and Binding Experiment

Myc-tagged and HA-tagged proteins were synthesized in vitro using the TNT SP6 High-Yield Wheat Germ Protein Expression System (Promega). Myc-tagged proteins were incubated with HA-tagged proteins at 4°C for 30 min then immunoprecipitated using c-Myc (9E10) AC beads (Santa Cruz Biotechnology). Immunoprecipitations were stringently washed with buffer [25mM Tris pH 7.5, 150mM NaCl, 2mM MgCl₂, 1% Triton X-100] and eluted with NuPAGE sample buffer (Invitrogen). Eluates were run on 4%-12% polyacrylamide gradient gels, immunoblotted with an anti-HA antibody (Covance) and anti-Myc (9E10).

siRNA Transfections, qRT-PCR, and Immunofluorescence

IMCD3 cells were cultured in DMEM: F12 1:1/10% FBS, and reverse transfected with 50 nM On-TargetPlus siRNA murine-specific oligos (Dharmacon) using Lipofectamine RNAimax (Invitrogen) onto acid-washed coverslips or glass-bottom 24-well multiwell plates (Greiner Bio). Cells were fixed at 72 hr in 4% paraformaldehyde in BRB80 buffer (80mM Pipes pH 6.8, 1mM MgCl₂, 1mM EDTA) and permeabilized with 0.2% Triton X-100 in PBS. Fixed cells were blocked with 5% cold fish gelatin in PBS for 40 min, incubated with primary antibodies mouse anti-acetylated a-tubulin (Sigma, T7451), and rabbit anti-pericentrin (Covance, PRB-432C) for 1 hr and secondary antibodies (Cy3 goat anti-rabbit, Cy3 goat anti-mouse, Cy5 goat anti-rabbit, or Cy5 goat anti-mouse) for 30 min. Cells were counterstained with Hoechst 33258 and stored in 80% Glycerol (plates). Coverslips were mounted on slides using ProLong Gold antifade reagent (Invitrogen). For immunostainings using ODF1, ODF2 and NPHP6 antibodies, cells were fixed in methanol (-20°C) for 5min, blocked with 5% cold fish gelatin in PBS for 40 min, and then incubated with primary antibodies [ODF1 (provided by Jeremy Reiter), ODF2 (Santa cruz N-20), or NPHP6 (Bethyl IHC-00365)], and secondary antibodies using the standard protocol. Fluorescence microscopy was performed on Marianas inverted microscope system (Intelligent Imaging Innovations, Inc.) equipped with a Zeiss Axiovert 200M microscope, a Cascade 512B camera, an environmental control chamber, and a Zeiss 63 × (NA 1.4) or Zeiss 40x (NA 1.3) PlanApochromat objective. Images were acquired and deconvolved using Slidebook 4.2 or Slidebook 5.0 (Intelligent Imaging Solutions).

The most potent siRNA duplex was selected after assessment of mRNA knockdown by qRT-PCR ([Figure S5](#); [Table S6](#)). For qRT-PCR, total RNA was prepared with the RNeasy Mini kit (QIAGEN). RNA (100 ng) was used for qRT-PCR by using TaqMan One-step RT-PCR Master Mix kit and TaqMan probes (Applied Biosystems). Triplicate reactions were run and analyzed on an ABI 7500 thermocycler.

3D Cell Culture and Immunofluorescence

IMCD3 cells were cultured and reverse transfected with 50 nM On-TargetPlus siRNA murine-specific oligos (Dharmacon) using Lipofectamine RNAimax (Invitrogen). 24 hr post transfection, 24-well plastic culture dishes were pretreated with 400 µl 4mg/mL collagen in medium, 0.25M NaHCO₃, and placed at 37°C for 30 min. Cells were trypsinized and resuspended cells were then mixed 1:1 with growth factor-depleted Matrigel (BD Bioscience) and layered on top of the collagen bed. After the Matrigel polymerized for 20 min at 37°C, warm medium was dropped over the matrix until just covered. IMCD3 cells formed spheroids with cleared lumens 3 days later.

Medium was removed and the gels were washed with warm PBS supplemented with calcium and magnesium. Gels were then transferred to 70mm nylon cell strainers (BD Falcon) and fixed in fresh 4% PFA for 30 min RT and gentle agitation. After washing with PBS, the cells were permeabilized for 15 min in gelatin dissolved in warm PBS (350mg/50mL) and 0.5% Triton X-100. Primary antibodies [rabbit anti- β -catenin (AHO0462, Invitrogen, 1:500), rat anti-ZO1 (R40.76, Santa Cruz Biotechnology, 1:500), and mouse anti-acetylated tubulin (T7451, Sigma, 1:20000)] were diluted in the permeabilization gelatin buffer and incubated at 4°C overnight. After washing the spheroids 3 times for 30 min in permeabilization buffer, secondary antibodies (donkey anti-mouse-Cy5 1:500, donkey anti-rabbit 488 1:500, and donkey-anti-rat Cy3 1:500, all purchased from Millipore) were also diluted in permeabilization buffer and incubated overnight at 4°C. The next day, spheroids were washed 3 times in permeabilization buffer and mounted with Hoechst (1:2000) on a coverslip in Fluoroumount-G (Cell Lab, Beckman Coulter). Images were taken with a Zeiss LSM510 upright confocal microscope. For spheroid defects, we first defined the sphericity of a spheroid using the three measurements of radii (R), which were sampled on each spheroid at 100 degree intervals. We then calculated the coefficient of variation (CV) using the formula: CV = standard deviation (R1,R2,R3) / mean (R1,R2,R3). A “defective” spheroid was called when CV > 15%.

Gli-Luciferase Assay

The Gli-luciferase assay was performed in S12 cells (C3H10T1/2 osteoblasts stably expressing a Hh-responsive Gli-luciferase reporter with 9x Gli binding sites), as previously described (Frank-Kamenetsky et al., 2002; Evangelista et al., 2008). Briefly, 8000 S12 cells were reverse-transfected for 48h with 100nM single or pooled siRNA and 0.3 μ L Dharmafect 2 transfection reagent (Dharmacon) in a single well of 96-well plate, followed by 24 hr serum starvation (0.5% FBS) in the presence or absence of 200 ng/ml octyl-Hh. Luciferase expression was detected with a Steadylite HTS kit (Perkin Elmer) and measured with a Top Count Luminometer (ABI).

Research Subject Recruitment and Linkage Analysis

Research Subjects

We obtained blood samples and pedigree information after obtaining informed consent from individuals with nephronophthisis or Joubert syndrome. Approval for human subject research was obtained from the University of Michigan Institutional Review Board. The diagnosis of NPHP or Joubert syndrome was based on published clinical criteria.

Linkage Analysis

For genome-wide homozygosity mapping, the GeneChip Human Mapping 250K Sty Array from Affymetrix was used. Non-parametric lod scores were calculated using a modified version of the program GENEHUNTER through stepwise use of a sliding window with sets of 110 SNPs and the program ALLEGRO to identify regions of homozygosity as described using a disease allele frequency of 0.0001 and CEU marker allele frequencies (Hildebrandt et al., 2009b).

Zebrafish Gene Knockdown and Analysis of Kupffer's Vesicle

Zebrafish gene orthologs were identified and Morpholino antisense oligonucleotides (MOs) were designed and purchased from Gene Tools. MO sequences are found in Table S7. MOs were microinjected into one to four cell stage embryos. Embryos were scored for the size of the Kupffer's Vesicle (KV) at the 8-12 somite stage. Embryos with KV smaller than the width of the notochord or with absent KV were scored as abnormal. Live embryos were photographed using a stereoscope with a Zeiss Axiocam camera.

Tctn2 Knockout Construction

Homologous arms were generated by PCR of DNA from E14 embryonic stem (ES) cells and cloned into pCR2.1. The long (5') arm was modified with the insertion of a loxP site 612 bp upstream of the first exon. Correctly sequenced arms were then cloned into a derivative of ploxPNT with loxP-flanked puromycin and diphtheria toxin A cassettes (DTA) (Figure S7). Linearized targeting vector was electroporated into KST296 E14 ES cells that have a gene trap in the first intron of *Tctn1* (Reiter and Skarnes, 2006). *Tctn1* and *Tctn2* are genetically linked so this was done to facilitate the analysis of double knockouts. ES cells were selected with puromycin and DTA and a total of 288 colonies were picked and expanded for analysis by long range PCR using the Roche Expand Long High Fidelity kit and the following primers: (3' arm) 5'TCCACTCCACTGTCCTC3' and 5'TGCTCAGTTCCCTGCATTG3'; (5' arm) 5'CCCCCATTTCTCTCCTCTC3' and 5'GGCTTGACTCGGTGATGGT3'.

PCR products from both arms were cloned and sequenced in their entirety to ensure proper targeting. Four of 288 clones were positive for homologous recombination by PCR, and these four clones and one negative control were subjected to Southern blot analysis using a 357 bp probe 5' of the targeted region. All four clones were verified as positive. Two of these clones were injected into C57Bl6 blastocysts and chimeras were backcrossed to C57Bl6 to verify germline transmission. Both clones gave identical phenotypes as described in the text. Yolk sac DNA was used for embryo genotyping using a primer set: 5'tgccaacccgtaaacacgtta3', 5'acgggtgcctacatccaag3', and 5'gctgatggcctgggtcta3'.

Histology and Immunofluorescence

For histology, embryos were fixed with Bouin's overnight and processed for paraffin sectioning using standard procedures. For immunofluorescence, E9.5 embryos were fixed in 4% paraformaldehyde for one hour, embedded in Optimal Cutting Temperature (OCT, TissueTek) and cryosectioned at 12 mm. Sections were blocked with 5% donkey serum and incubated overnight with primary antibodies at 4°C followed by 1:1000 Alexa-conjugated secondary antibodies for one hour at room temperature. Mouse embryonic

fibroblasts (MEFs) were grown to confluence on glass coverslips and starved in OptiMEM for 24 hr to induce cilia formation prior to fixation in 4% paraformaldehyde for ten minutes. Sections and cells were mounted with ProLong Gold with DAPI (Molecular Probes) and imagined with a Leica SP5 confocal microscope. Post-acquisition image processing was done with MetaMorph software. Antibodies used were: rabbit anti-Pax6 (1:300, Covance), mouse anti-Pax3, Islet1/2, and FoxA2 (all 1:20, Developmental Studies Hybridoma Bank), mouse anti-acetylated tubulin (1:5000, Sigma), rabbit anti-Arl13b (1:5000, gift from Tamara Caspary), and rabbit anti-Ninein (1:20,000, gift from James Sillibourne).

MEF Derivation, qPCR, and Western Blot

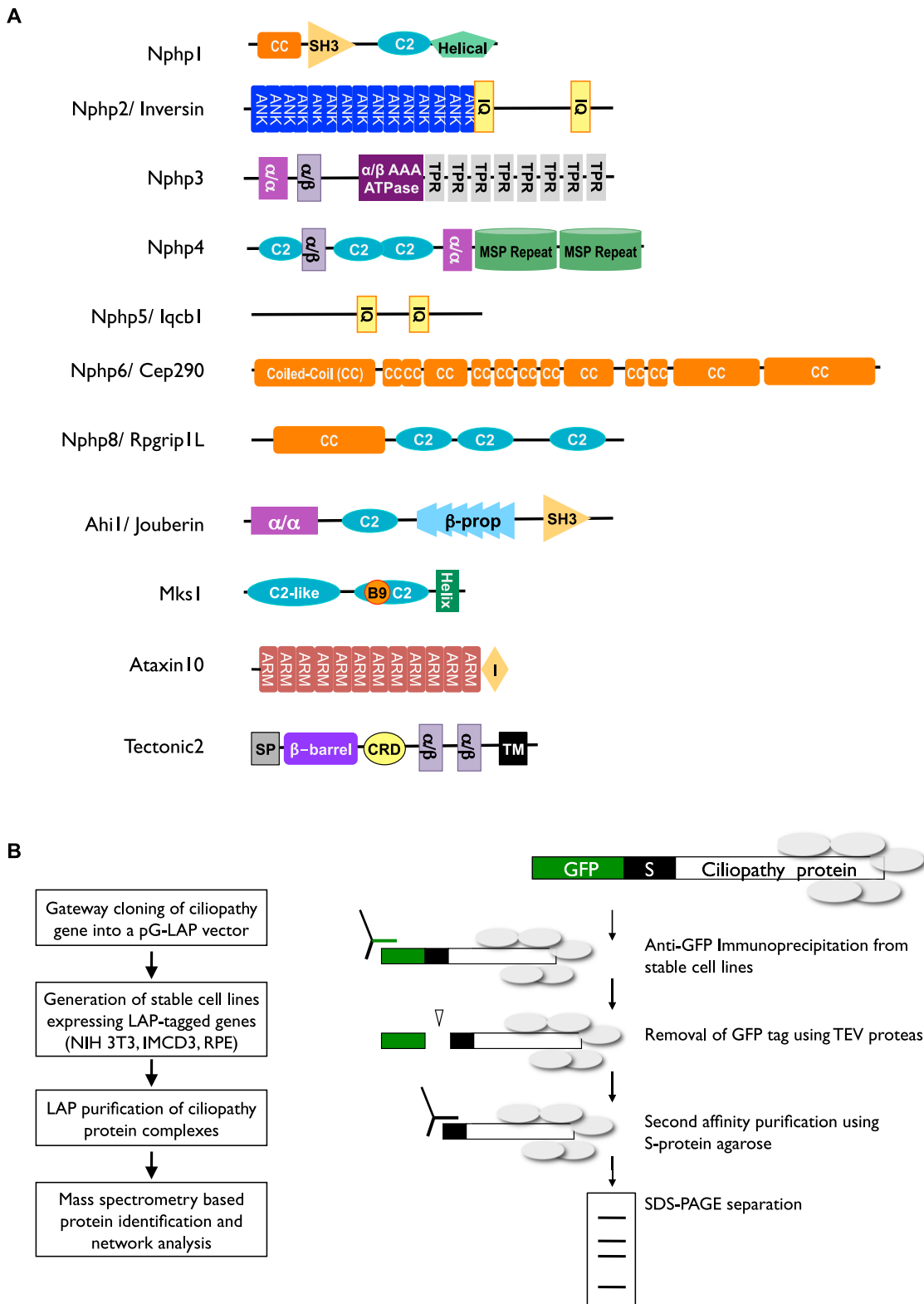
Mouse embryonic fibroblasts (MEFs) were derived from E12.5 embryos as described (Corbit et al., 2008). MEFs were grown to in 48 wells to confluence and starved in OptiMEM for 24 hr to induce cilia formation prior to addition of DMSO or 5 uM Smoothened agonist (SAG, Axxora) for 18 hr. RNA was extracted with RNeasy (QIAGEN) and first strand cDNA synthesized using the iScript kit (BioRad). qPCR was carried out with the SYBR Green/Rox master mix (Fermentas) on an ABI 7300 machine. The following primers were used: β-actin F (CACAGCTTCTTGAGCTCCTT); β-actin R (CGTCATCCATGGCGAACTG); Gli1 F (CTTCACCCCTGCCATGAAACT); Gli1 R (TCCAGCTGAGTGTTGTCCAG); Ptc1 F (TGATTGTGGAAGGCCACAGAAAA); Ptc1 R (TGTCTGGAGTCCGGATGGA).

For immunoblot, E12.5 embryos were homogenized with a razor blade and protein extracted with 1 ml of RIPA with Protease Inhibitor Cocktail (Set III, EMD Biosciences). 20 µg of protein from each embryo was separated by 7% SDS-PAGE and probed with 1:5000 mouse anti-Gli3 (6F5). A mixed CD1/Bl6 wild-type cross was used for the Atxn10 Western, while pure Bl6 heterozygotic crosses were used for Tctn2 Western. Embryonic brain and kidney were isolated and immediately dropped into liquid nitrogen. After evaporation of all liquid the tissue was ground with a mortar and pestle to a powder. For ‘total lysate’ the remaining carcass (after brain and kidney dissection) was treated the same. Tissue powder was reconstituted in 1 ml RIPA (50 mM Tris pH 7.4 with 150 mM NaCl, 1% Triton X-100, 1% NP-40 and 0.1% SDS supplemented with protease and phosphatase inhibitors). 50 ug of total lysate was resolved for the Atxn10 Westerns (used at 1:2000; Proteintech 15693-1-AP), which were stripped and re-probed with mouse monoclonal anti-alpha tubulin (Sigma T9026) at 1:5000. For Tctn2, 1 mg of lysate either E14.5 kidneys or brain were immunoprecipitated with 20 ul rabbit anti-TCTN2 (Proteintech 17053-1-AP) overnight at 4C. Immunoprecipitates were collected with 20 ul of packed rProteinG agarose (Invitrogen 15920-010) for 1 hr at 4C. Immunocomplexes were washed 3 × 1 ml RIPA and 1 × 1 ml PBS, resolved by SDS-PAGE and probed with rabbit anti-Tctn2 (ProSci, Inc. 5835) at 1:1000.

SUPPLEMENTAL REFERENCES

- Alexa A., Rahnenfuhrer J. (2009). topGO: Enrichment analysis for Gene Ontology. R package version 1.16.2.
- Arts, H.H., Doherty, D., van Beersum, S.E., Parisi, M.A., Letteboer, S.J., Gorden, N.T., Peters, T.A., Märker, T., Voesenek, K., Kartono, A., et al. (2007). Mutations in the gene encoding the basal body protein RPGRIP1L, a nephrocystin-4 interactor, cause Joubert syndrome. *Nat. Genet.* 39, 882–888.
- Attanasio, M., Uhlenhaut, N.H., Sousa, V.H., O'Toole, J.F., Otto, E., Anlag, K., Klugmann, C., Treier, A.C., Helou, J., Sayer, J.A., et al. (2007). Loss of GLIS2 causes nephronophthisis in humans and mice by increased apoptosis and fibrosis. *Nat. Genet.* 39, 1018–1024.
- Bergmann, C., Fliegauf, M., Brüchle, N.O., Frank, V., Olbrich, H., Kirschner, J., Schermer, B., Schmedding, I., Kispert, A., Kränzlin, B., et al. (2008). Loss of nephrocystin-3 function can cause embryonic lethality, Meckel-Gruber-like syndrome, situs inversus, and renal-hepatic-pancreatic dysplasia. *Am. J. Hum. Genet.* 82, 959–970.
- Bielas, S.L., Silhavy, J.L., Brancati, F., Kisseleva, M.V., Al-Gazali, L., Sztriha, L., Bayoumi, R.A., Zaki, M.S., Abdel-Aleem, A., Rosti, R.O., et al. (2009). Mutations in INPP5E, encoding inositol polyphosphate-5-phosphatase E, link phosphatidyl inositol signaling to the ciliopathies. *Nat. Genet.* 41, 1032–1036.
- Bisgrove, B.W., and Yost, H.J. (2006). The roles of cilia in developmental disorders and disease. *Development* 133, 4131–4143.
- Boxem, M., Maliga, Z., Klitgord, N., Li, N., Lemmens, I., Mana, M., de Lichtervelde, L., Mul, J.D., van de Peut, D., Devos, M., et al. (2008). A protein domain-based interactome network for *C. elegans* early embryogenesis. *Cell* 134, 534–545.
- Briscoe, J., Sussel, L., Serup, P., Hartigan-O'Connor, D., Jessell, T.M., Rubenstein, J.L., and Ericson, J. (1999). Homeobox gene Nkx2.2 and specification of neuronal identity by graded Sonic hedgehog signalling. *Nature* 398, 622–627.
- Cantagrel, V., Silhavy, J.L., Bielas, S.L., Swistun, D., Marsh, S.E., Bertrand, J.Y., Audollent, S., Attié-Bitach, T., Holden, K.R., Dobyns, W.B., et al; International Joubert Syndrome Related Disorders Study Group. (2008). Mutations in the cilia gene ARL13B lead to the classical form of Joubert syndrome. *Am. J. Hum. Genet.* 83, 170–179.
- Corbit, K.C., Shyer, A.E., Dowdle, W.E., Gaulden, J., Singla, V., Chen, M.H., Chuang, P.T., and Reiter, J.F. (2008). Kif3a constrains beta-catenin-dependent Wnt signalling through dual ciliary and non-ciliary mechanisms. *Nat. Cell Biol.* 10, 70–76.
- Davis, E.E., Brueckner, M., and Katsanis, N. (2006). The emerging complexity of the vertebrate cilium: new functional roles for an ancient organelle. *Dev. Cell* 11, 9–19.
- Dessaud, E., McMahon, A.P., and Briscoe, J. (2008). Pattern formation in the vertebrate neural tube: a sonic hedgehog morphogen-regulated transcriptional network. *Development* 135, 2489–2503.
- Dixon-Salazar, T., Silhavy, J.L., Marsh, S.E., Louie, C.M., Scott, L.C., Gururaj, A., Al-Gazali, L., Al-Tawari, A.A., Kayserili, H., Sztriha, L., and Gleeson, J.G. (2004). Mutations in the AHI1 gene, encoding jouberin, cause Joubert syndrome with cortical polymicrogyria. *Am. J. Hum. Genet.* 75, 979–987.
- Donaldson, J.C., Dise, R.S., Ritchie, M.D., and Hanks, S.K. (2002). Nephrocystin-conserved domains involved in targeting to epithelial cell-cell junctions, interaction with filamins, and establishing cell polarity. *J. Biol. Chem.* 277, 29028–29035.
- Ericson, J., Rashbass, P., Schedl, A., Brenner-Morton, S., Kawakami, A., van Heyningen, V., Jessell, T.M., and Briscoe, J. (1997). Pax6 controls progenitor cell identity and neuronal fate in response to graded Shh signaling. *Cell* 90, 169–180.

- Evangelista, M., Lim, T.Y., Lee, J., Parker, L., Ashique, A., Peterson, A.S., Ye, W., Davis, D.P., and de Sauvage, F.J. (2008). Kinome siRNA screen identifies regulators of ciliogenesis and hedgehog signal transduction. *Sci. Signal.* 1, ra7.
- Frank-Kamenetsky, M., Zhang, X.M., Bottega, S., Guicherit, O., Wichterle, H., Dudek, H., Bumcrot, D., Wang, F.Y., Jones, S., Shulok, J., et al. (2002). Small-molecule modulators of Hedgehog signaling: identification and characterization of Smoothened agonists and antagonists. *J. Biol.* 7, 10.
- Gorden, N.T., Arts, H.H., Parisi, M.A., Coene, K.L.M., Letteboer, S.J.F., van Beersum, S.E.C., Mans, D.A., Hikida, A., Eckert, M., Knutzen, D., et al. (2008). CC2D2A is mutated in Joubert syndrome and interacts with the ciliopathy-associated basal body protein CEP290. *Am. J. Hum. Genet.* 83, 559–571.
- Hildebrandt, F., Heeringa, S.F., Rüschendorf, F., Attanasio, M., Nürnberg, G., Becker, C., Seelow, D., Huebner, N., Chernin, G., Vlangos, C.N., et al. (2009). A systematic approach to mapping recessive disease genes in individuals from outbred populations. *PLoS Genet.* 5, e1000353.
- Hildebrandt, F., and Otto, E. (2005). Cilia and centrosomes: a unifying pathogenic concept for cystic kidney disease? *Nat. Rev. Genet.* 6, 928–940.
- Hildebrandt, F., Otto, E., Rensing, C., Nothwang, H.G., Vollmer, M., Adolphs, J., Hanusch, H., and Brandis, M. (1997). A novel gene encoding an SH3 domain protein is mutated in nephronophthisis type 1. *Nat. Genet.* 17, 149–153.
- Hildebrandt, F., and Zhou, W. (2007). Nephronophthisis-associated ciliopathies. *J. Am. Soc. Nephrol.* 18, 1855–1871.
- Jacoby, M., Cox, J.J., Gayral, S., Hampshire, D.J., Ayub, M., Blockmans, M., Pernot, E., Kisileva, M.V., Compère, P., Schiffmann, S.N., et al. (2009). INPP5E mutations cause primary cilium signaling defects, ciliary instability and ciliopathies in human and mouse. *Nat. Genet.* 41, 1027–1031.
- Kyttilä, M., Tallila, J., Salonen, R., Kopra, O., Kohlschmidt, N., Paavola-Sakki, P., Peitonen, L., and Kestilä, M. (2006). MKS1, encoding a component of the flagellar apparatus basal body proteome, is mutated in Meckel syndrome. *Nat. Genet.* 38, 155–157.
- Lancaster, M.A., Louie, C.M., Silhavy, J.L., Sintasath, L., Decambre, M., Nigam, S.K., Willert, K., and Gleeson, J.G. (2009). Impaired Wnt-beta-catenin signaling disrupts adult renal homeostasis and leads to cystic kidney ciliopathy. *Nat. Med.* 15, 1046–1054.
- Letunic, I., Doerks, T., and Bork, P. (2009). SMART 6: recent updates and new developments. *Nucleic Acids Res.* 37 (Database issue), D229–D232.
- McGuffin, L.J., Bryson, K., and Jones, D.T. (2000). The PSIPRED protein structure prediction server. *Bioinformatics* 16, 404–405.
- Novick, P., Field, C., and Schekman, R. (1980). Identification of 23 complementation groups required for post-translational events in the yeast secretory pathway. *Cell* 21, 205–215.
- O'Brien, L.E., Zegers, M.M., and Mostov, K.E. (2002). Opinion: Building epithelial architecture: insights from three-dimensional culture models. *Nat. Rev. Mol. Cell Biol.* 3, 531–537.
- Otto, E., Hoefele, J., Ruf, R., Mueller, A.M., Hiller, K.S., Wolf, M.T., Schuermann, M.J., Becker, A., Birkenhäger, R., Sudbrak, R., et al. (2002). A gene mutated in nephronophthisis and retinitis pigmentosa encodes a novel protein, nephroretinin, conserved in evolution. *Am. J. Hum. Genet.* 71, 1161–1167.
- Otto, E.A., Loey, B., Khanna, H., Hellemans, J., Sudbrak, R., Fan, S., Muerb, U., O'Toole, J.F., Helou, J., Attanasio, M., et al. (2005). Nephrocystin-5, a ciliary IQ domain protein, is mutated in Senior-Loken syndrome and interacts with RPGR and calmodulin. *Nat. Genet.* 37, 282–288.
- Otto, E.A., Trapp, M.L., Schultheiss, U.T., Helou, J., Quarmby, L.M., and Hildebrandt, F. (2008). NEK8 mutations affect ciliary and centrosomal localization and may cause nephronophthisis. *J. Am. Soc. Nephrol.* 19, 587–592.
- Parisi, M.A., Bennett, C.L., Eckert, M.L., Dobyns, W.B., Gleeson, J.G., Shaw, D.W., McDonald, R., Eddy, A., Chance, P.F., and Glass, I.A. (2004). The NPHP1 gene deletion associated with juvenile nephronophthisis is present in a subset of individuals with Joubert syndrome. *Am. J. Hum. Genet.* 75, 82–91.
- Praetorius, H.A., and Spring, K.R. (2003). The renal cell primary cilium functions as a flow sensor. *Curr. Opin. Nephrol. Hypertens.* 12, 517–520.
- Ross, A.J., May-Simera, H., Eichers, E.R., Kai, M., Hill, J., Jagger, D.J., Leitch, C.C., Chapple, J.P., Munro, P.M., Fisher, S., et al. (2005). Disruption of Bardet-Biedl syndrome ciliary proteins perturbs planar cell polarity in vertebrates. *Nat. Genet.* 37, 1135–1140.
- Rual, J.F., Venkatesan, K., Hao, T., Hirozane-Kishikawa, T., Dricot, A., Li, N., Berriz, G.F., Gibbons, F.D., Dreze, M., Ayivi-Guedehoussou, N., et al. (2005). Towards a proteome-scale map of the human protein-protein interaction network. *Nature* 437, 1173–1178.
- Sayer, J.A., Otto, E.A., O'Toole, J.F., Nurnberg, G., Kennedy, M.A., Becker, C., Hennies, H.C., Helou, J., Attanasio, M., Fausett, B.V., et al. (2006). The centrosomal protein nephrocystin-6 is mutated in Joubert syndrome and activates transcription factor ATF4. *Nat. Genet.* 38, 674–681.
- Simons, M., Gloy, J., Ganner, A., Bullerkotte, A., Bashkurov, M., Krönig, C., Schermer, B., Benzing, T., Cabello, O.A., Jenny, A., et al. (2005). Inversin, the gene product mutated in nephronophthisis type II, functions as a molecular switch between Wnt signaling pathways. *Nat. Genet.* 37, 537–543.
- Smith, U.M., Consugar, M., Tee, L.J., McKee, B.M., Maina, E.N., Whelan, S., Morgan, N.V., Goranson, E., Gissen, P., Lillquist, S., et al. (2006). The transmembrane protein meckelin (MKS3) is mutated in Meckel-Gruber syndrome and the wpk rat. *Nat. Genet.* 38, 191–196.
- Söding, J. (2005). Protein homology detection by HMM-HMM comparison. *Bioinformatics* 21, 951–960.
- Spektor, A., Tsang, W.Y., Khoo, D., and Dynlacht, B.D. (2007). Cep97 and CP110 suppress a cilia assembly program. *Cell* 130, 678–690.
- Tanabe, Y., Roelink, H., and Jessell, T.M. (1995). Induction of motor neurons by Sonic hedgehog is independent of floor plate differentiation. *Curr. Biol.* 5, 651–658.
- Torres, J.Z., Miller, J.J., and Jackson, P.K. (2009). High-throughput generation of tagged stable cell lines for proteomic analysis. *Proteomics* 9, 2888–2891.
- Tsang, W.Y., Bossard, C., Khanna, H., Peränen, J., Swaroop, A., Malhotra, V., and Dynlacht, B.D. (2008). CP110 suppresses primary cilia formation through its interaction with CEP290, a protein deficient in human ciliary disease. *Dev. Cell* 15, 187–197.
- Valente, E.M., Logan, C.V., Mougou-Zerelli, S., Lee, J.H., Silhavy, J.L., Brancati, F., Iannicelli, M., Travaglini, L., Romani, S., Illi, B., et al. (2010). Mutations in TMEM216 perturb ciliogenesis and cause Joubert, Meckel and related syndromes. *Nat. Genet.* 42, 619–625.
- Wang, B., Fallon, J.F., and Beachy, P.A. (2000). Hedgehog-regulated processing of Gli3 produces an anterior/posterior repressor gradient in the developing vertebrate limb. *Cell* 100, 423–434.
- Wolfrum, U., and Schmitt, A. (2000). Rhodopsin transport in the membrane of the connecting cilium of mammalian photoreceptor cells. *Cell Motil. Cytoskeleton* 46, 95–107.
- Wu, S., and Zhang, Y. (2008). MUSTER: Improving protein sequence profile-profile alignments by using multiple sources of structure information. *Proteins* 72, 547–556.
- Zhou, W., Dai, J., Attanasio, M., and Hildebrandt, F. (2010). Nephrocystin-3 is required for ciliary function in zebrafish embryos. *Am. J. Physiol. Renal Physiol.* 299, F55–F62.

**Figure S1. Related to Figure 1**

(A) Modular architecture of NPHP-JBTS-MKS proteins. The domain composition of the diverse set of NPHP, JBTS and MKS proteins was first probed with SMART (Letunic et al., 2009). For chain segments that defied SMART categorization but were suggested by PsiPRED (McGuffin et al., 2000) to be likely globular

domains rich in secondary structure, more sensitive fold recognition methods like HHPRED (Söding, 2005) and MUSTER (Wu and Zhang, 2008) were employed to define a possible domain relationship and function by structural homology. In cases where the suggested fold is uncertain, only the fold type is noted (e.g., α/α or α/β).

(B) Schematic of the G-LAP-Flp technology. Ciliopathy genes were inserted into pG-LAP vectors containing an EGFP-TEV-S peptide coding sequence and an FRT targeting site for Flp recombinase-mediated integration into a mammalian cell line. Complexes associated with each cystoprotein were immunopurified from stable cell lines using anti-GFP antibody beads, eluted with TEV protease and recaptured on S-protein agarose. Eluates were separated on SDS-polyacrylamide gels and interacting proteins were identified by mass spectrometry.

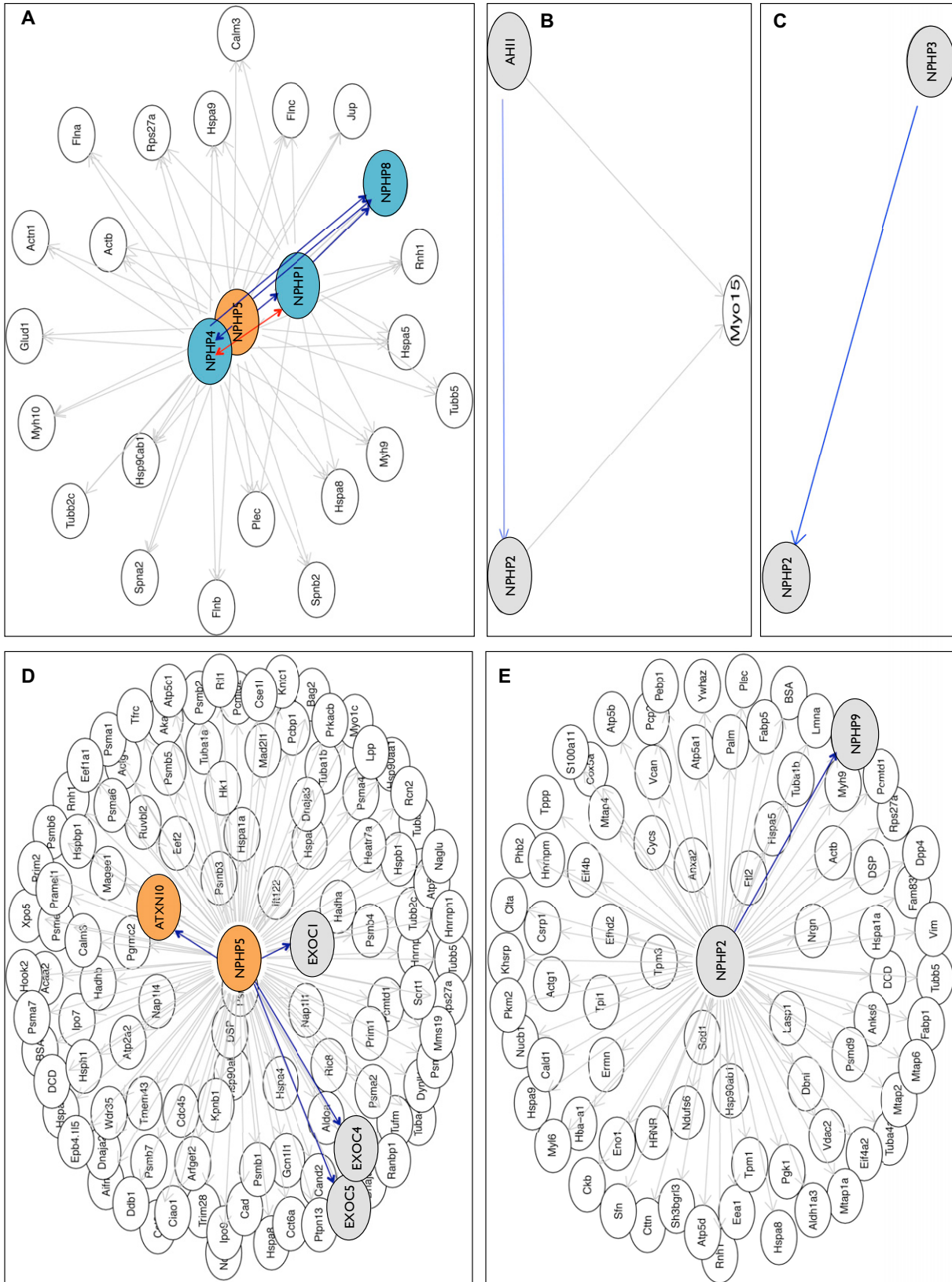


Figure S2. Related to Figure 1

Network diagrams generated using the R script showing the Multi-Bait, Multi-Edge (MBME), Single Bait, Multi-Hits (SBMH) and Unreciprocated Bait-Bait (UnRBB) subgraphs in each network.

(A–C) NIH 3T3 subgraphs.

(D–E) IMCD3 subgraphs. Ellipse = protein; single headed arrows = unreciprocated interactions (pointing to the hits); double headed arrows (red) = reciprocal interactions. The bait proteins and a subset of interactors are highlighted using the color scheme described in [Figure 1B](#).

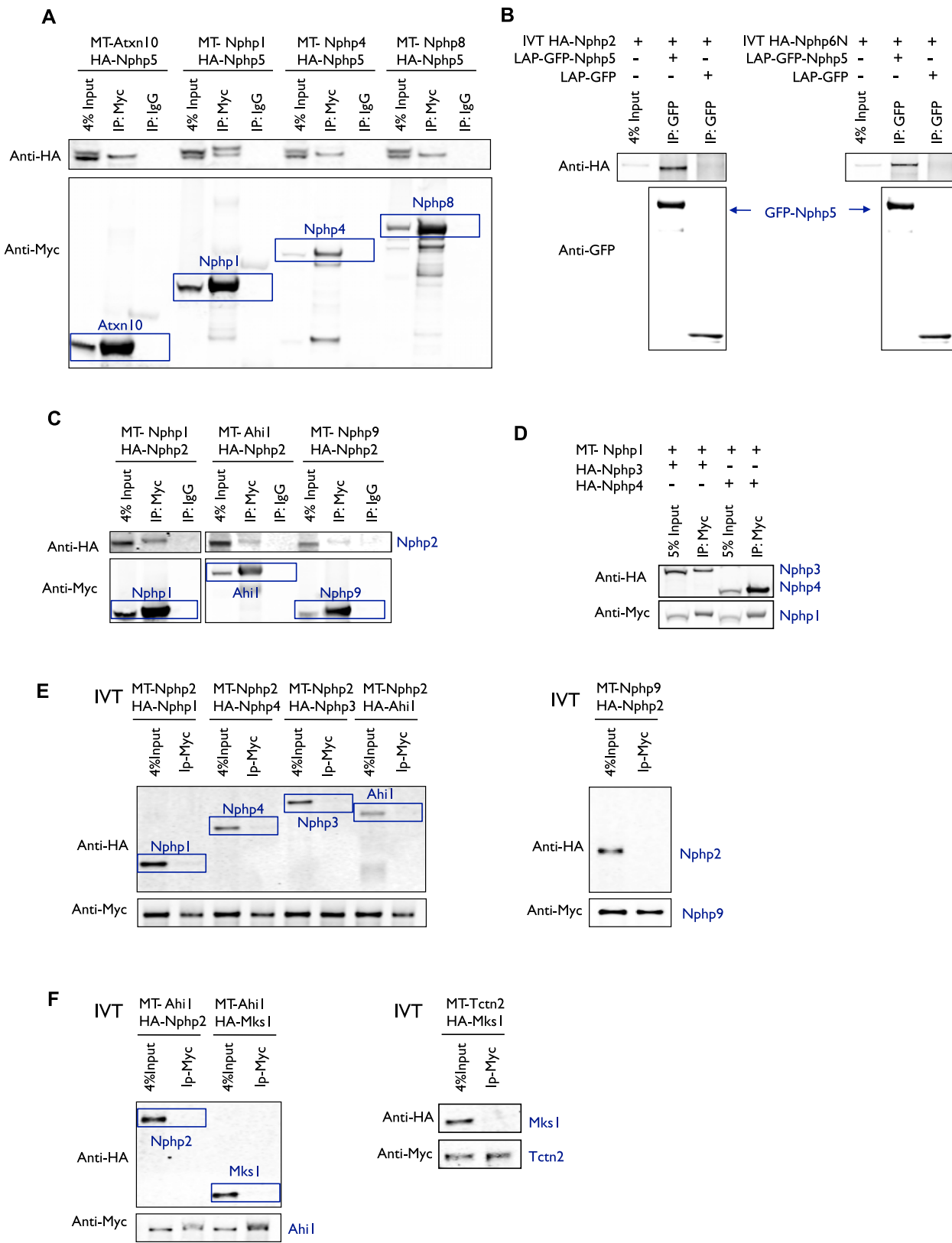


Figure S3. Related to Figure 2

(A and B) Validation of the interactions between Nphp5 and copurified proteins.

(A) HA-tagged Nphp5 was coexpressed with MT-tagged Atxn10, Nphp1, Nphp4 or Nphp8 in HEK293T cells and immunoprecipitated using anti-Myc beads or control IgG beads. Eluates were separated by SDS-PAGE and immunoblotted with an anti-HA antibody.

(B) LAP-GFP-Nphp5 or LAP-GFP ctrl was immunopurified from IMCD3 cells using anti-GFP beads, and incubated with in vitro translated HA-tagged Nphp2 or an N-terminal fragment of Nphp6 (Nphp6N). Eluates were separated by SDS-PAGE and immunoblotted with an anti-HA antibody.

(C) Validation of the interactions between Nphp2 and copurified proteins. HA-tagged Nphp2 was coexpressed with MT-tagged Nphp1, Ahi1 or Nphp9 in HEK293T cells and immunoprecipitated using anti-Myc beads or control IgG beads. Eluates were separated by SDS-PAGE and immunoblotted with an anti-HA antibody.

(D) NPHP1 co-purifies with Nphp3 and Nphp4 from HEK293T cells. MT-tagged Nphp1 was coexpressed with HA-tagged Nphp3 or Nphp4 in HEK293T cells and immunoprecipitated using anti-Myc beads. Eluates were separated by SDS-PAGE and immunoblotted with an anti-HA antibody.

(E) Nphp2 doesn't bind directly to Nphp1, Nphp4, Nphp3, Ahi11 or Nphp9 in vitro. Myc-tagged or HA-tagged Nphp2, Nphp1, Nphp4, Nphp3, Ahi1 and Nphp9 were in vitro translated using wheat germ extract. Each Myc-tagged protein was incubated with HA-tagged protein and immunoprecipitated using anti-Myc beads. Eluates were separated by SDS-PAGE and immunoblotted with an anti-HA antibody.

(F) Mks1 doesn't bind directly to Ahi1 or Tctn2 in vitro. HA-tagged Mks1 and Myc-tagged Ahi1 and Tctn2 were in vitro translated using wheat germ extract, co-incubated and immunoprecipitated using anti-Myc beads. Eluates were separated by SDS-PAGE and immunoblotted with an anti-HA antibody.

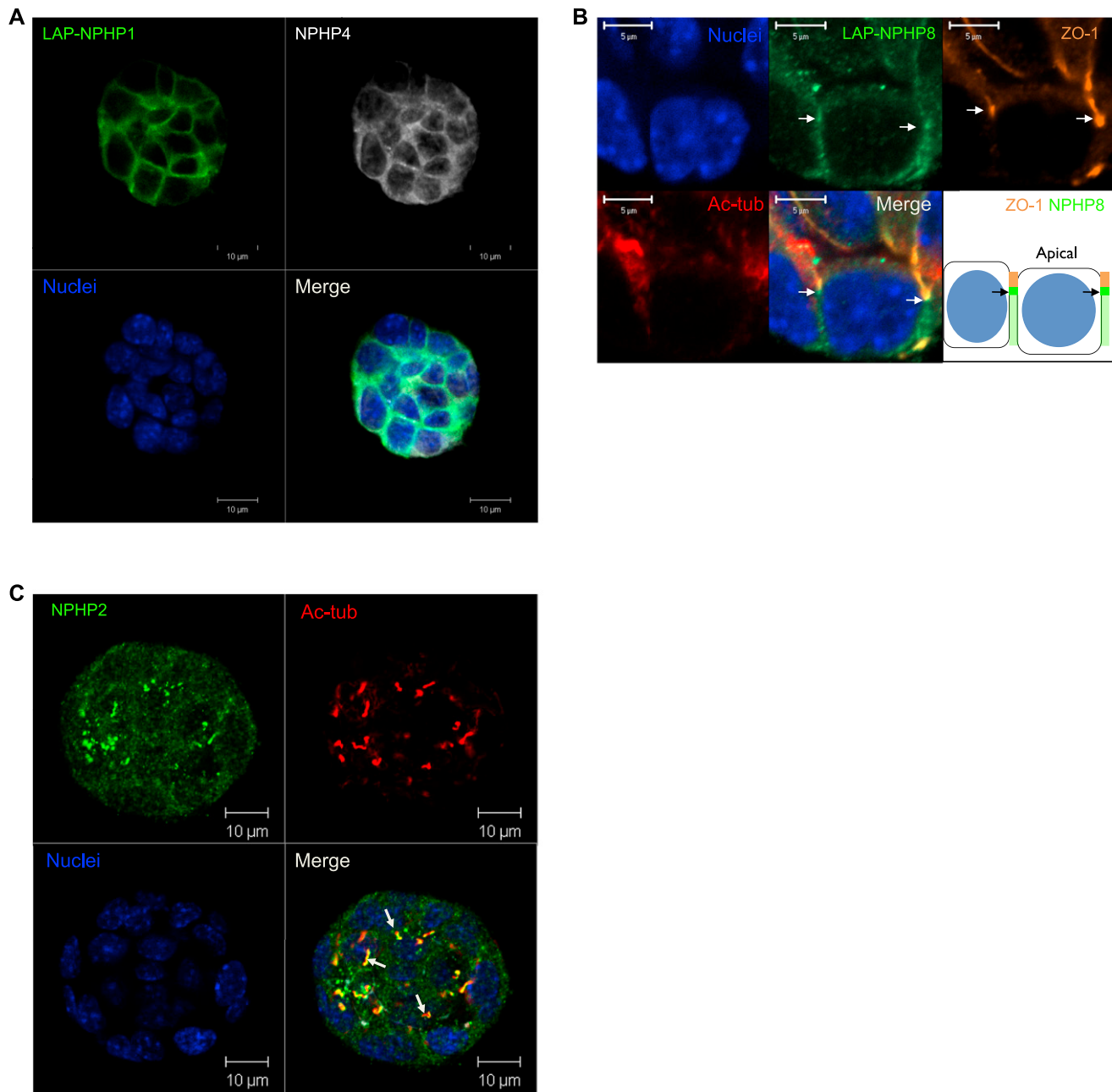


Figure S4. Related to Figure 3 and Figure 4

(A) Co-localization of NPHP1 and NPHP4. IMCD3 spheroids stably expressing LAP-NPHP1 (green) were immunostained for NPHP4 (white).

(B) IMCD3 cells stably expressing LAP-NPHP8 (green) were immunostained for ZO1 (brown) and acetylated α -tubulin (ac-tub, red). Nuclei were stained with Hoechst 33528 (blue). NPHP8 localizes basolateral of ZO1, as illustrated in the cartoon.

(C) NPHP2 localizes to the cilium. IMCD3 spheroids were immunostained for NPHP2 (green) and acetylated α -tubulin (ac-tub, red). Nuclei were stained with Hoechst 33528. Arrows exemplify variable extensions along the axoneme.

Scale bars, 10um (A) and (C), 5um (B).

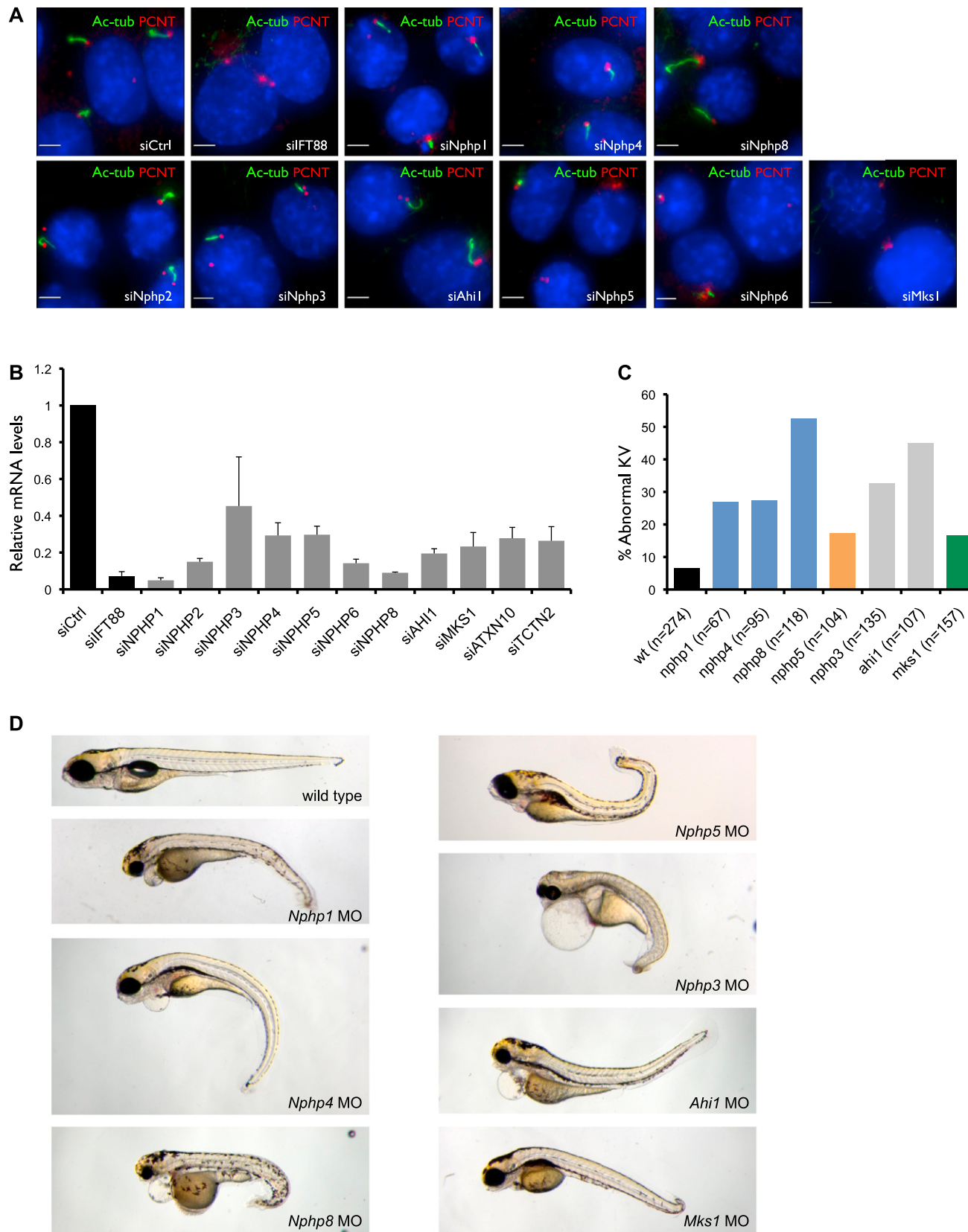


Figure S5. Related to Figure 4

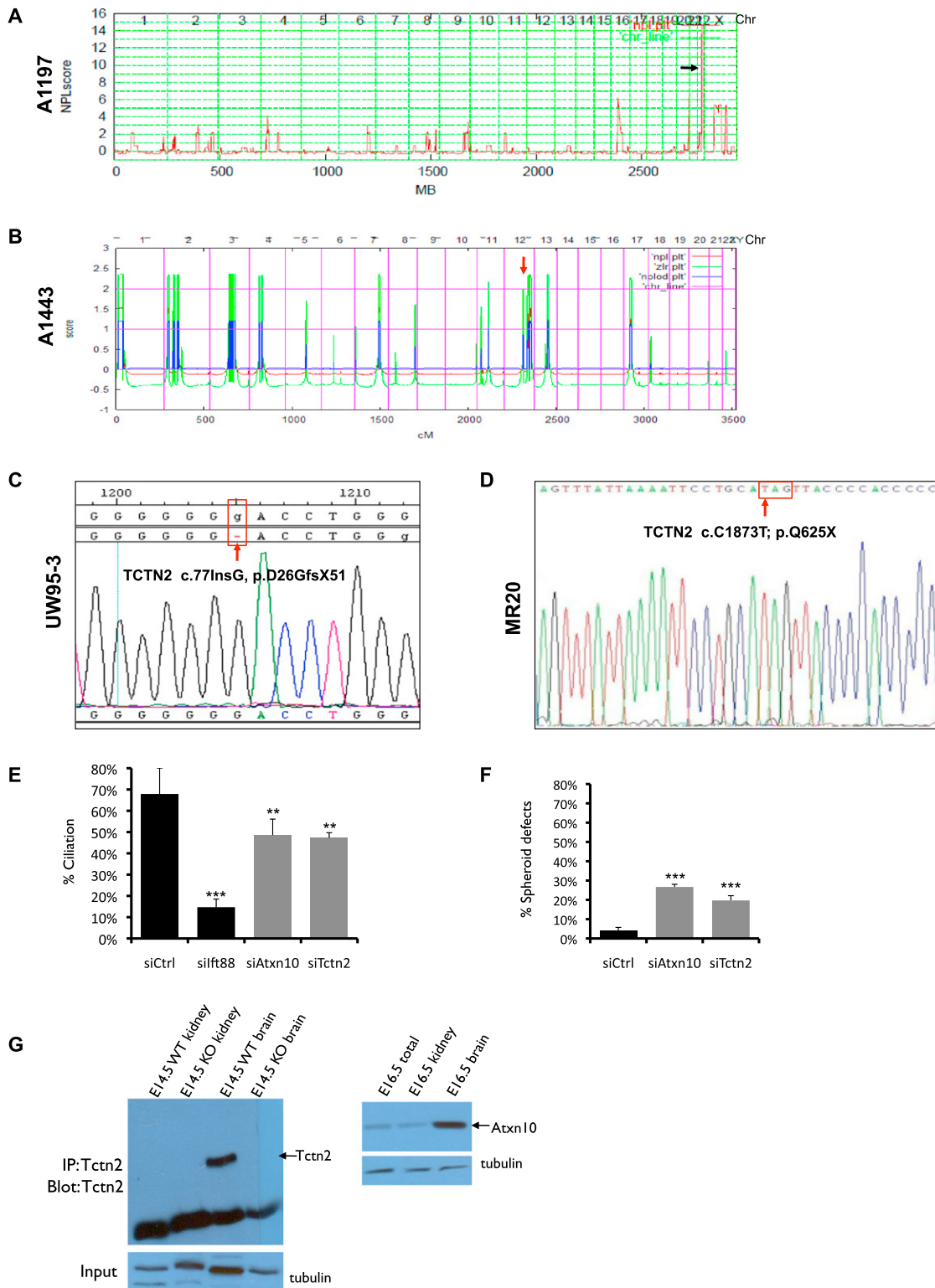
(A) Depletion of IFT88, NPHP5, NPHP6, and MKS1 cause ciliation defects. IMCD3 cells were transfected with siRNAs against individual disease genes, IFT88, or control. Cells were fixed 72 hr post-transfection and stained for acetylated α -tubulin (green), pericentrin (red), and DNA dye Hoechst 33528 (blue). A representative image from each knockdown was shown. Scale bar, 5 μ m.

(B) Efficiency of siRNA-mediated depletion of NPHP-JBTS-MKS genes compared to non-targeting siRNA (siCtrl) was assessed using qRT-PCR. Error bars represent standard error.

(C and D) Knockdown of NPHP-JBTS-MKS genes in zebrafish.

(C) Knockdown of NPHP-JBTS-MKS genes results in Kupffer's Vesicle (KV) defects scored at the 8-12 somite stage. $p < 0.01$, Fisher's exact test.

(D) Side view of 5 day post fertilization wild-type and Morpholino injected embryos. Knockdown of NPHP-JBTS-MKS genes leads to curved or misshaped body axis.

**Figure S6. Related to Figure 5**

(A) Non-parametric lod (NPL) scores across the human genome in three siblings with nephronophthisis of consanguineous family A1197. The x-axis shows Affymetrix 250K Sty array SNP positions on human chromosomes concatenated from *p*-ter (left) to *q*-ter (right). Three maximum NPL peaks indicate candidate regions of homozygosity by descent. Mutation analysis in *ATXN10* on chromosome 22 (arrow) resulted in the identification of a splice site mutation (IVS8-3T > G).

- (B) Whole genome linkage analysis in a single patient of family A1443 resulted in 13 maximum NPL peaks. Mutation analysis revealed an obligatory splice site mutation (IVS10-1G > A) in *TCTN2* on chromosome 12 (arrow).
- (C and D) Chromatograms of patient mutations in *TCTN2*. (C) Frameshift mutation “c.771InsG” in patient UW95-3 and (D) nonsense mutation “c.C1873T” in family MR20 are noted.
- (E) Depletion of Atxn10 and Tctn2 cause modest ciliation defects. IMCD3 cells were transfected with siRNAs against Atxn10, Tctn2, Ift88, or control. Cells were fixed 72 hr later and immunostained for acetylated α-tubulin and pericentrin, and scored for % nuclei with cilia (500-700 cells counted). Error bars represent standard error. **p < 0.01; ***p < 0.001 (student's t test).
- (F) Depletion of Atxn10 and Tctn2 result in modest lumen defects in 3D Spheroids (400-700 spheroids counted). Error bars represent standard error. ***p < 0.001 (student's t test).
- (G) Expression of Tctn2 and Atxn10 in mouse embryonic kidney and brain tissues. Tissue lysate from Tctn2 WT and KO mouse embryonic kidneys (E14.5) or brain (E14.5) were immunoprecipitated using anti-TCTN2 beads. Eluates were separated by SDS-PAGE and immunoblotted with an anti-Tctn2 antibody. Tissue lysates from E16.5 mouse embryos (total), kidneys or brain were immunoblotted with an anti-Atxn10 antibody.

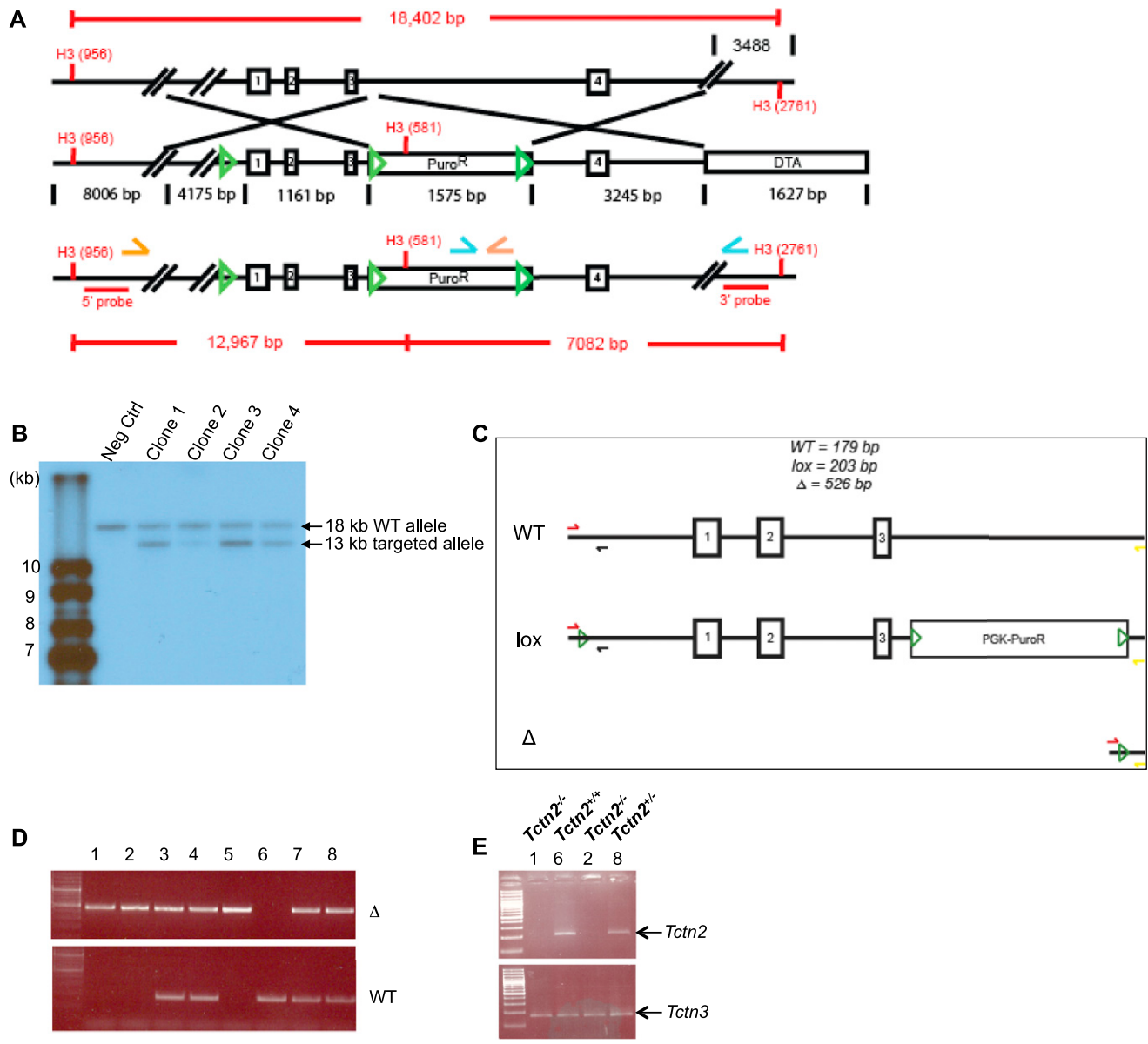


Figure S7. *Tctn2* Knockout Construction, Related to Figure 6

(A) Schematic of *Tctn2* targeting strategy. 18.4 kb of the *Tctn2* locus is shown encompassing the first four exons. 5336 and 3245 bp homologous arms were cloned between a *loxP*-flanked puromycin-resistance cassette. The DTA gene was cloned downstream of the right homologous arm for negative selection. A single *loxP* site was placed 612 bp upstream of the first exon. A correctly-targeted integration is shown in the bottom panel. Long range PCR using primers within the puromycin-resistance cassette used in conjunction with primers outside of the targeted region served as a first-pass screen for homologous recombinants (orange and blue arrow heads).

(B) HindIII (H3) digestion followed by Southern blot was used to confirm homologous recombination. Southern blot of HindIII-digested DNA from clones scored positive by long-range PCR (and one negative control) hybridized with a 5' probe. The wild-type ~18 kb band is present in all clones, while the ~13 kb band specific for homologous recombinants is found in the four clones scored positive by long-range PCR. Size in kilobases is given on the side.

(C) Schematic of genotyping strategy to distinguish wild-type, targeted (Lox), and knockout (D) alleles post Cre-excision.

(D) Genotyping of a single E9.5 litter from a *Tctn2*^{+/+}:*bactinCre* intercross using the strategy outlined in (C). The knockout and wild-type (WT) products are shown.

(E) RT-PCR of E9.5 embryos demonstrates loss of *Tctn2* in *Tctn2*^{-/-} embryos. *Tctn3* was used as control. The numbers correspond to the same embryos used for genotyping in (D).